

1 **Technical Note: Constraining the hydroxyl (OH) radical in the tropics with satellite observations of its**
2 **drivers: First steps toward assessing the feasibility of a global observation strategy**

3
4 Daniel C. Anderson^{1,2}, Bryan N. Duncan², Julie M. Nicely^{2,3}, Junhua Liu^{2,4}, Sarah A. Strode^{2,4}, Melanie B.
5 Follette-Cook⁵

- 6
7 1. GESTAR II, University of Maryland Baltimore County, Baltimore, MD, USA
8 2. Atmospheric Chemistry and Dynamics Laboratory, NASA Goddard Space Flight Center, Greenbelt,
9 MD, USA
10 3. Earth System Science Interdisciplinary Center, University of Maryland, College Park, MD, USA
11 4. GESTAR II, Morgan State University, Baltimore, MD, USA
12 5. Mesoscale Atmospheric Processes Laboratory, NASA Goddard Space Flight Center, Greenbelt, MD,
13 USA

14
15 *Correspondence to:* Daniel C. Anderson (daniel.c.anderson@nasa.gov)

16
17 **Abstract**

18 Despite its importance in controlling the abundance of methane (CH₄) and a myriad of other
19 tropospheric species, the hydroxyl radical (OH) is poorly constrained due to its large spatial
20 heterogeneity and the inability to measure tropospheric OH with satellites. Here, we present a
21 methodology to infer tropospheric column OH (TCOH) in the tropics over the open oceans using a
22 combination of a machine learning model, output from a simulation of the GEOS model, and satellite
23 observations. Our overall goals are to assess the feasibility of our methodology, to identify potential
24 limitations, and to suggest areas of improvement in the current observational network. The
25 methodology reproduces the variability of TCOH from independent 3D model output and of
26 observations from the Atmospheric Tomography mission (ATom). While the methodology also
27 reproduces the magnitude of the 3D model validation set, the accuracy of the magnitude when applied
28 to observations is uncertain because current observations are insufficient to fully evaluate the machine
29 learning model. Despite large uncertainties in some of the satellite retrievals necessary to infer OH,
30 particularly for NO₂ and HCHO, current satellite observations are of sufficient quality to apply the
31 machine learning methodology, resulting in an error comparable to that of *in situ* OH observations.
32 Finally, the methodology is not limited to a specific suite of satellite retrievals. Comparison of TCOH
33 determined from two sets of retrievals does show, however, that systematic biases in NO₂, resulting
34 both from retrieval algorithm and instrumental differences, lead to relative biases in the calculated
35 TCOH. Further evaluation of NO₂ retrievals in the remote atmosphere is needed to determine their
36 accuracy. With slight modifications, a similar methodology could likely be expanded to the extra-tropics
37 and over land, with the benefits of increasing our understanding of the atmospheric oxidation capacity
38 and, for instance, informing understanding of recent CH₄ trends.

39
40 **1 Introduction**

41 The hydroxyl radical (OH) dictates the lifetime of many tropospheric species, including carbon monoxide
42 (CO), methane (CH₄), and numerous volatile organic compounds (VOCs). Knowledge of OH is therefore
43 necessary to understand the abundance, distribution, and variability of these species. For instance,
44 Rigby et al. (2017) and Laughner et al. (2021) attribute recent trends and increases in CH₄ at least
45 partially to changes in OH abundance. Current constraints on OH are insufficient, however, to assess its
46 relative importance in controlling these trends (Turner et al., 2017).

48 Differences in OH distributions among chemistry transport (CTM) and chemistry climate models (CCM)
49 suggest that these models are insufficient to inform understanding of OH abundance and variability
50 without further observational constraints. OH abundance can differ by up to 80% among models
51 constrained with identical emissions in intercomparison projects (Voulgarakis et al., 2013; Nicely et
52 al.; Zhao et al., 2019; Murray et al., 2021), with modeled trends disagreeing with those derived from
53 observationally constrained methods (Stevenson et al., 2020). Variables such as the photolysis
54 frequency of O₃ (JO¹D) (Nicely et al., 2020), the NO_x lifetime (NO_x = NO + NO₂), and the oxidation
55 efficiency of VOCs (Murray et al., 2021) contribute to these inter-model variations in OH. Using
56 Gaussian emulation, Wild et al. (2020) found that the relative importance of drivers of OH variability
57 differed widely among three CTMs. Likewise, the response of OH to the El Niño Southern Oscillation
58 (ENSO), the dominant mode of OH variability on monthly and seasonal timescales (e.g. Anderson et al.,
59 2021; Turner et al., 2018), and other modes of internal climate variability can vary widely among models
60 (Anderson et al., 2021).

61
62 Despite this need for better constraints, observations of tropospheric OH are limited. The hydroxyl
63 radical has a lifetime of approximately 1s (Mao et al., 2009), resulting in large spatial heterogeneity in
64 both the horizontal and vertical. This spatial heterogeneity is further caused by the large variation in the
65 relative importance of drivers of OH loss and production in different regions of the atmosphere (e.g.
66 Spivakovsky et al., 1990; Lelieveld et al., 2016). A strategic, representative in situ observational network
67 is therefore unfeasible. As a result, observations of OH are generally limited to intensive field campaigns
68 (Miller and Brune, 2022) that have narrow spatial and temporal coverage. While remotely-sensed OH
69 observations are available, those from satellites are limited to the stratosphere (e.g., Pickett et al.,
70 2008), while ground-based observations of total column OH are dominated by the stratospheric
71 contribution (e.g., Burnett and Minschwaner, 1998).

72
73 Reference gases with well-characterized sources and an OH sink, such as methyl chloroform (MCF), can
74 be used to infer OH abundance (Lovelock, 1977). This methodology, however, generally yields no
75 information on spatial heterogeneity beyond the hemispheric scale (e.g., Montzka et al., 2011; Rigby et
76 al., 2017; Naus et al., 2019), although there has been recent success when using three dimensional
77 inversion techniques (Naus et al., 2021). For MCF in particular, recent declines in tropospheric
78 abundance will soon dictate the need for a new reference species (Liang et al., 2017).

79
80 Multiple studies have attempted to constrain OH through the creation of proxies and the application of
81 satellite retrievals of OH drivers. Murray et al. (2014) showed that global OH strongly correlated with a
82 combination of JO¹D, water vapor (H₂O_(v)), and the tropospheric sources of reactive nitrogen and carbon
83 in the GEOS-Chem model. Murray et al. (2021) demonstrated that OH correlated with this proxy in
84 multiple CTMs, although the relationship differs strongly among models. Miyazaki et al. (2020) created
85 a data assimilation framework that ingested satellite observations of CO, NO₂, O₃, and HNO₃ (nitric acid)
86 into multiple CTMs. The data assimilation reduced the spread in average OH among the models and
87 brought the interhemispheric ratio closer to unity, in line with values suggested by MCF observations
88 (e.g. Patra et al., 2014). These results demonstrate that the incorporation of satellite observations into a
89 modeling framework can improve the representation of OH. Wolfe et al. (2019) developed a proxy for
90 OH based on formaldehyde (HCHO) production and loss rates. They applied that proxy to satellite HCHO
91 observations to estimate OH columns in the remote troposphere, a region where HCHO abundance is
92 low and the satellite retrievals are reflective of the *a priori* (Zhu et al., 2016). Using machine learning,
93 chemical transport model output, and retrievals of NO₂ and HCHO, Zhu et al. (2022b) developed a
94 method to estimate surface OH in North American urban areas. Finally, Pimlott et al. (2022) used a
95 steady state approximation of OH, including primary production from H₂O and O₃ and loss from CO, CH₄,

96 and O₃, to estimate OH between 600 and 700 hPa using observations from IASI (Infrared Atmospheric
97 Sounding Interferometer). A logical next step, building on the results of these studies, is the
98 development of a methodology to constrain OH that ingests multiple satellite retrievals, encompasses
99 the breadth of OH chemical and dynamical drivers, and spans a significant enough portion of the globe
100 to inform variability and trends in CH₄ and CO loss.

101
102 Combining machine learning, chemical transport model (CTM) output, and satellite data has the
103 potential to constrain tropospheric column OH (TCOH). A variety of machine learning techniques, such
104 as neural networks (Nicely et al., 2017; Nicely et al., 2020; Kelp et al., 2020), self-organizing maps
105 (Stauffer et al., 2016), random forest regression (Keller and Evans, 2019), and gradient boosted
106 regression trees (GBRTs) (Ivatt and Evans, 2020; Zhu et al., 2022b; Anderson et al., 2022) show promise in
107 helping to solve problems in atmospheric chemistry. In particular, Zhu et al. (2022b) and Anderson et al.
108 (2022) demonstrated the ability of GBRTs to predict OH from a chemical transport model with
109 reasonable accuracy. GBRT models (Elith et al., 2008; Chen and Guestrin, 2016) use an ensemble of
110 decision trees to predict the value of a target based on multiple inputs, even for targets with highly non-
111 linear dependencies on the inputs.

112
113 Here, we present a methodology to infer clear sky TCOH in the tropics from space-based observations of
114 its chemical and dynamical drivers with the goal of assessing the feasibility of our methodology,
115 identifying potential limitations, and suggesting areas of improvement in the current observational
116 network. We train a GBRT model using output from a simulation of the NASA GEOS (Goddard Earth
117 Observing System) model, and then estimate TCOH in the actual atmosphere at the satellite overpass
118 time using inputs from a suite of satellite retrievals. In Section 2, we describe the methodology for
119 generating the machine learning model as well as the satellite retrievals used to constrain TCOH. We
120 then evaluate the suitability of MERRA2 GMI as a training dataset (Sect. 3) and, in Section 4, present a
121 satellite-constrained OH product for one month from each season. Finally, in Section 5, we explore
122 potential methodological limitations and benefits, including lack of validation data, the impacts of
123 observational uncertainties, and the ability to use different satellites and retrievals as inputs to the GBRT
124 model.

125
126 **2 Description of the methodology to generate the GBRT model and of the associated datasets**
127 Our overall aim is to demonstrate the feasibility of our approach to constrain TCOH with satellite-based
128 observations over broad regional scales. As a first step, we restrict our analysis to latitudes equatorward
129 of 25° and regions over water. We chose to focus initially on this domain as it has appreciable OH
130 concentrations and simplified chemistry, as compared to regions with large biogenic and anthropogenic
131 VOC emissions. Nevertheless, this portion of the atmosphere accounts for 50 – 60% of global CO and
132 CH₄ loss. In this section, we describe the creation of the machine learning model used to predict TCOH
133 (Sect. 2.1) for this region as well as the satellite products used as inputs to the machine learning model
134 (Sect. 2.2).

135

136 **2.1 Creation of the TCOH model**

137 **2.1.1 Creation of the GBRT training dataset**

138 For the machine learning model training dataset, we use a subset of output from the MERRA2 GMI
139 simulation (<https://acd-ext.gsfc.nasa.gov/Projects/GEOSCCM/MERRA2GMI/>). MERRA2 GMI is a 40 year
140 (1980 – 2019) simulation of the NASA GEOS model run in replay mode (Orbe et al., 2017) with MERRA2
141 (Modern Era Retrospective analysis for Research and Applications, version 2) meteorology (Gelaro et al.,
142 2017). The simulation has a resolution of c180 on the cubed sphere (approximately 0.625° longitude by
143 0.5° latitude) with 72 vertical layers and uses the Global Modeling Initiative (GMI) chemical mechanism

144 (Duncan et al., 2007; Strahan et al., 2007). Output is available at daily- and monthly-averaged resolution,
 145 as well as instantaneous values at 10:00 and 14:00 LST. These times are within approximately 30
 146 minutes of the overpass times of the satellites described in Section 2.2. Anderson et al. (2021) and
 147 Strode et al. (2019) provide detailed information about the simulation, including emissions.

148
 149 The training target for the machine learning model is TCOH. In Anderson et al. (2022), we developed a
 150 GBRT parameterization trained on MERRA2 GMI output to predict in situ OH concentrations using 27
 151 inputs, only a small fraction of which are observable from space. That parameterization, designed to be
 152 integrated into the GEOS modeling framework, performed better when there was a separate model for
 153 each month as opposed to one model for all months. While that GBRT model is not appropriate for the
 154 application described here, we employ a similar approach, creating a separate set of TCOH training
 155 targets for each month. We use instantaneous OH output from MERRA2 GMI at 14:00 local time for
 156 each day of a given month across the years 2005 to 2019, a timeframe that maximizes overlap between
 157 the operational lifetime of the satellites listed in Table 1 and the period of the MERRA2 GMI simulation.
 158 We omitted data from 2017 to evaluate model performance. For a given month and year, we calculate
 159 daily tropospheric column values across the grid, filtering out columns where the maximum cloud
 160 fraction in that column was greater than 30% in order to align the training targets more closely with
 161 satellite data, where retrievals of some species are often filtered for cloud cover. This yields
 162 approximately 43,000 valid grid boxes per day. For each year, we then average these values to monthly
 163 resolution. This results in approximately 600,000 total training targets for each month over the 15-year
 164 period.

165
 166 **Table 1:** Input variables to the machine learning model and the corresponding satellite retrieval used to create the
 167 satellite OH product. Overpass times are ~13:30 LST for all satellites except MOPITT, which has a 10:30 LST
 168 overpass.

Variable	Satellite retrieval	Original horizontal and temporal resolution	Reference
Total O ₃ column	OMI TOMS-Like L3 version 3	0.25° × 0.25°, daily	McPeters et al. (2015)
Tropospheric NO ₂ column	OMI GSFC L3 version 4	0.25° × 0.25°, daily	Lamsal et al. (2021)
CO column	MOPITT L3 version 8	1.0° × 1.0°, monthly	Deeter et al. (2019)
HCHO column	OMI SAO L3 version 3	0.1° × 0.1°, daily	González Abad et al. (2015)
H ₂ O _(v) column	AIRS L3 version 6	1.0° × 1.0°, monthly	Susskind et al. (2014)
Sea surface temperature	MUR L4 version 4.2	0.25° × 0.25°, daily	Chin et al. (2017)
Aerosol optical depth at 550 nm	MODIS Aqua L3 collection 6	0.5° × 0.5°, daily	Levy et al. (2013)
H ₂ O _(v) layers: 925 – 850 hPa, 850 – 700 hPa, 700 – 600 hPa, 600 – 500 hPa, 500 – 400 hPa, 400 – 300 hPa, and 300 - 250 hPa	AIRS L3 version 6	1.0° × 1.0°, monthly	Susskind et al. (2014)
Solar zenith angle	N/A		
Latitude	N/A		

169
 170 We selected the input variables for the machine learning model (Table 1) based on their relevance to OH
 171 chemistry and variability as well as our current ability to observe the variable with satellites.

172 Performance was similar for a model including total column ozone only and for a model also including
 173 the tropospheric column. We therefore use total column ozone because of the uncertainties inherent in

174 separating the column into two parts in the satellite retrieval. We chose the water vapor layers to
175 correspond with the Atmospheric Infrared Sounder (AIRS) layers product. Layers are averages over the
176 indicated pressure range, and we denote the layer names by the highest pressure in that range. We
177 include sea surface temperatures (SST) as a proxy for the Indian Ocean Dipole and ENSO, which has a
178 strong impact on OH variability in the tropics (Anderson et al., 2021; Turner et al., 2018; Naus et al.,
179 2021). In addition, we include latitude and solar zenith angle as previous work has shown that these
180 variables can explain a large fraction of the spatial OH variability (Duncan et al., 2000; Anderson et al.,
181 2022).

182
183 We sampled the MERRA2 GMI output to create the training dataset in the same manner as for the TCOH
184 targets. The inputs to the machine learning model each correspond to the same model column as the
185 OH target. All column values are instantaneous and taken from 14:00 to correspond with satellite
186 overpass times, except for CO, which is for 10:00, near the Measurement of Pollution in the
187 Troposphere (MOPITT) overpass time. Model performance was similar when using CO output at 14:00
188 and 10:00, likely because of limited diurnal variability in CO column in the study region. SSTs are
189 monthly averages of 24-hour averaged values, and we calculated solar zenith angle at the surface for
190 noon on the 15th of a given month.

191 192 **2.1.2 Creation and tuning of the GBRT model**

193 We used the XGBoost package (Chen and Guestrin, 2016) version 0.81 in Python version 3.6 to create a
194 GBRT model of TCOH for each month using the training datasets from MERRA2 GMI. For each month,
195 we used 90% of the dataset for model training and the remainder for model validation. As mentioned in
196 Section 2.1.1, we also used MERRA2 GMI output from 2017, which was omitted from the training
197 dataset, as further validation.

198
199 To maximize parameterization performance while also balancing the potential of overfitting, we tuned
200 hyperparameters, including the learning rate, the maximum tree depth, and the number of trees. We
201 chose hyperparameter values that minimized the parameterization root mean square error (RMSE) of
202 the training dataset. We set the learning rate, which controls the magnitude of change when adding a
203 new tree, to 0.1, while we varied the maximum tree depth and number of trees from 6 to 22 and from
204 10 to 150, respectively. For both maximum tree depth and number of trees, RMSE initially dropped
205 significantly with increasing value, representing sharp improvement in parameterization performance.
206 RMSE values eventually plateaued, increasing parameterization runtime without noticeably improving
207 performance. A combination of a maximum tree depth of 18 and 100 trees balanced performance with
208 model training and run time.

209
210 To determine whether the inputs to the machine learning model improved or hindered performance, we
211 performed a “leave one out” analysis. Using 5-fold cross validation, we retrained the model, individually
212 omitting each of the inputs, to determine the percent difference between the mean RMSE of the 5 folds
213 for the model without a specific input and one including all inputs. Omitting the inputs listed in Table 1
214 lead to increases in the RMSE, suggesting that each is necessary for improved model performance. As a
215 result of this analysis, we do not use water vapor layers for pressures less than 300 hPa because these
216 decreased model performance.

217
218 Finally, we found that it was not necessary to apply satellite averaging kernels and shape factors to the
219 training dataset. Of the satellite retrievals used in this work (discussed in Sect. 2.2 and listed in Table 1),
220 only CO, HCHO, and NO₂ could require convolving the model with the averaging kernel. Shape factors
221 for the OMI NO₂ retrieval are determined from a similar setup of the GEOS model, also employing the

222 GMI chemical mechanism and MERRA2 meteorology. Applying the satellite shape factors to the
223 simulation discussed here would therefore not result in significant changes in the modeled NO₂
224 (Anderson et al., 2021). To test whether it is necessary to apply the averaging kernels for CO and HCHO,
225 we created a separate training dataset, where we convolved the daily MERRA2 GMI output with the
226 averaging kernel and a priori from the level 2 data for both species for February 2005 - 2019. All other
227 inputs were kept the same. We then retrained the model with these adjusted CO and HCHO variables.
228 When we applied the satellite data to the model for February 2017, as described in Section 4, the
229 resulting TCOH differed by less than 1% on average from the model that did not include averaging kernel
230 information. This level of uncertainty is significantly smaller than the other uncertainties discussed in
231 Section 5, so we do not include averaging kernels in our analysis.

232

233 **2.2 Description of satellite products**

234 To create the observationally-constrained OH product, we use multiple satellite retrievals, listed in Table
235 1 and briefly described here. Each instrument is located onboard a polar orbiting satellite that provides
236 near global coverage daily. For each satellite retrieval, we use the level 3 gridded product, with the
237 exception of SST which is level 4. Where necessary, we regridded the retrieval to a common horizontal
238 grid with a resolution of 1.0° × 1.0° and averaged to the monthly scale.

239

240 We use these resolutions because, in the study domain, individual pixel retrievals, particularly of NO₂
241 and HCHO, are frequently at or below detection limits (González Abad et al., 2015; Lamsal et al., 2021),
242 necessitating averaging to relatively coarse temporal and spatial scales. Missing data due to cloud cover
243 and the Ozone Monitoring Instrument (OMI) row anomaly further increase the need for monthly-scale
244 averaging. While other satellites, such as OMPS (Ozone Mapping and Profiler Suite) and TROPOMI
245 (Tropospheric Monitoring Instrument), provide retrievals with increased signal to noise ratios and more
246 complete data coverage, the satellites used here cover a far longer time period. The 1.0° × 1.0° and
247 monthly resolutions, in combination with the long data record, are sufficient to understand regional
248 trends in TCOH and some aspects of TCOH temporal and spatial variability.

249

250 We use retrievals of three species – HCHO, O₃, and NO₂ – from OMI, an ultraviolet-visible spectrometer
251 located onboard the Aura satellite, which has an overpass of approximately 13:30 local solar time (LST).
252 We use the Smithsonian Astrophysical Observatory (SAO) version 3 HCHO retrieval (González Abad et
253 al., 2015). Wolfe et al. (2019) found that this retrieval captured the variability of the HCHO columns in
254 the remote atmosphere observed during the Atmospheric Tomography (ATom) campaign with little bias.
255 For total column O₃, we use the TOMS-like (Total Ozone Mapping Spectrometer) retrieval version 3
256 (McPeters et al., 2015), which agrees with ground-based and other satellite observations within
257 approximately 1% (Labow et al., 2013). Finally, we use the Goddard Space Flight Center version 4 NO₂
258 tropospheric column retrieval (Lamsal et al., 2021). While previous studies have thoroughly evaluated
259 this retrieval in more polluted atmospheres (e.g., Lamsal et al., 2014; Choi et al., 2020), evaluation in the
260 remote tropical atmosphere, as defined in this study, is limited.

261

262 For water vapor and aerosol optical depth (AOD) at 550 nm, we use retrievals from AIRS and the
263 Moderate Resolution Imaging Spectroradiometer (MODIS) instruments, respectively, both located
264 onboard the Aqua satellite with an overpass of approximately 13:30 LST. We use the total column water
265 vapor standard physical retrieval as well as the 7 water vapor layers listed in Table 1 (Susskind et al.,
266 2014). Multiple studies have evaluated the accuracy of the AIRS H₂O_(v) column and layers retrievals in
267 the remote tropical atmosphere, finding bias of 5% or less and high correlation against both remote and
268 *in situ* observations (Bedka et al., 2010; Anderson et al., 2016; Pérez-Ramírez et al., 2019). We use

269 collection 6 of the dark target MODIS AOD retrieval at 550 nm, which is highly correlated with
270 observations from the AERONET network over the ocean (Levy et al., 2013).

271
272 We also use retrievals of CO from MOPITT, which is onboard the Terra satellite with an overpass of
273 10:30 LST. We use the version 8 retrieval that includes both near and thermal infrared radiances (Deeter
274 et al., 2019). CO retrievals from MOPITT in the remote tropics generally agree with ground-based
275 remotely-sensed observations within 10% (Hedelius et al., 2019; Buchholz et al., 2017).

276
277 Finally, we use SSTs from the Multi-scale Ultra-high Resolution (MUR) analysis, which combines
278 nighttime SST observations from multiple satellite platforms, including MODIS, as well as *in situ*
279 observations and agrees with other SST analyses within 0.36° C (Chin et al., 2017).

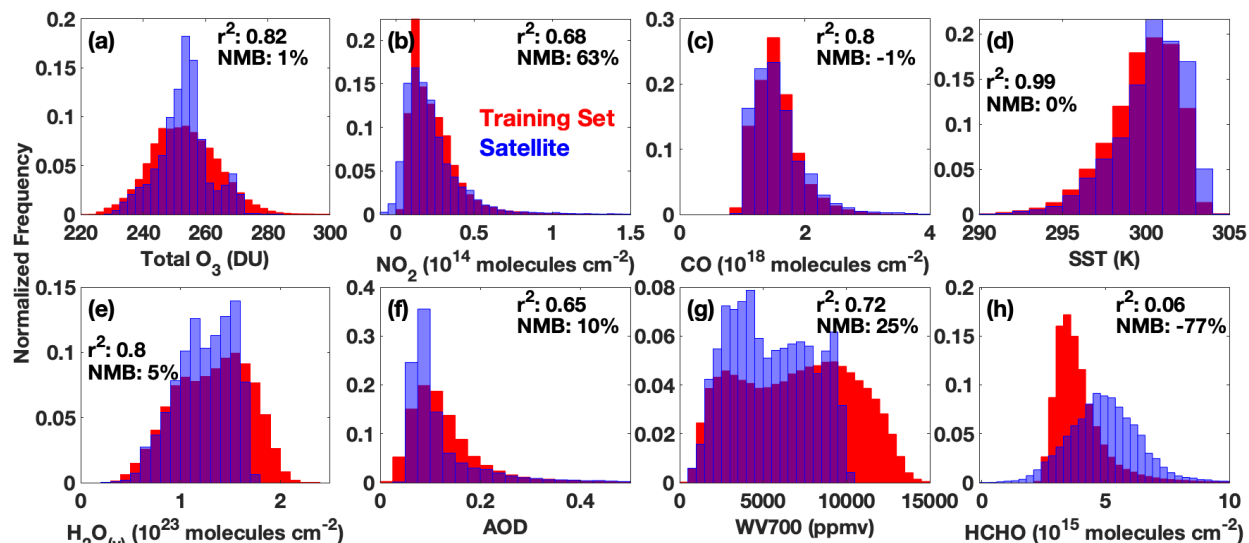
280 281 **3 Evaluating the Suitability of the MERRA2 GMI Simulation as a Training Dataset**

282 Before generating the GBRT model to predict TCOH, we first demonstrate that the MERRA2 GMI
283 simulation is suitable to use as a training dataset. Because of the paucity of *in situ* observations of OH
284 over most of the globe, we necessarily use output from an atmospheric chemistry model to train the
285 machine learning model. The atmospheric chemistry model output must reasonably capture the
286 distribution, magnitude, and ENSO-related variability of OH and the drivers listed in Table 1, as GBRT
287 models are unable to extrapolate beyond the photochemical environments on which they are trained
288 (Anderson et al., 2022).

289 290 **3.1 Comparison of the Distribution and Magnitude of Simulated OH Drivers to Observations**

291 Simulated OH from MERRA2 GMI agrees with observations over the remote ocean within the
292 instrumental uncertainty. Anderson et al. (2021) compared MERRA2 GMI output to *in situ* observations
293 from the first two deployments of ATom, finding modest correlation (r^2 values between 0.3 and 0.78
294 depending on the hemisphere and season) between observations and the model. The average
295 normalized mean bias was on the order of 20%, a slight high bias but within the 2σ observational
296 uncertainty of 35%. Agreement was highest in the remote atmosphere, whereas the largest error was in
297 regions of fresh, continental outflow off the coasts of South America and New Zealand.

298



299
300 **Figure 1:** Comparison of the normalized distributions of the training dataset (red) for the February model and
301 satellite observations of the indicated species for February 2017 (blue). Purple indicates regions of overlap. We

302 use $\text{H}_2\text{O}_{(\text{v})}$ at 700 hPa as an example for all $\text{H}_2\text{O}_{(\text{v})}$ layers. Distributions of the other $\text{H}_2\text{O}_{(\text{v})}$ layers are shown in Figure
303 S1. We also indicate the r^2 of the correlation between MERRA2 GMI output for February 2017 and the
304 corresponding satellite retrieval as well as the normalized mean bias of that output.

305 The simulation captures both the observed variability and the magnitude of the majority of GBRT model
306 inputs with reasonable fidelity, suggesting that the satellite retrievals highlighted in Section 2.2 are
307 suitable inputs for a machine learning model trained on MERRA2 GMI output (Fig.1). Figure 1 compares
308 the distribution of the February training dataset created from the MERRA2 GMI simulation for 2005 –
309 2019 to the satellite observations of the indicated species for February 2017, a month omitted from the
310 training dataset. Distributions of the remaining water vapor layers are shown in Figure S1. In addition,
311 correlations between observations and MERRA2 GMI output for February 2017 are shown, as an
312 example, in Figures S2 and S3. With the exception of HCHO, distributions of the species are similar
313 between the observations and MERRA2 GMI, with the training dataset encompassing the full range of
314 almost all species. A GBRT model trained on MERRA2 GMI will therefore likely not have to extrapolate
315 to photochemical environments on which it was not trained when applied to the satellite data. Further,
316 MERRA2 GMI total column O_3 , $\text{H}_2\text{O}_{(\text{v})}$ column, AOD, CO, and SSTs are all highly correlated (r^2 of 0.65 or
317 higher) with their respective satellite observations, and biases are within 10%, on average. Anderson et
318 al. (2021) did show that MERRA2 GMI CO columns demonstrate biases of opposite sign in the Northern
319 and Southern Hemispheres, however.

320
321 Agreement between MERRA2 GMI and satellite observations for NO_2 , HCHO, and the $\text{H}_2\text{O}_{(\text{v})}$ layers is
322 more variable than for the other species. While modeled NO_2 is moderately correlated with
323 observations ($r^2 = 0.68$) with relatively similar distributions, MERRA2 GMI has a NMB of 63%. This
324 disagreement is most pronounced at low column values, however, where observational uncertainty is
325 large. Further, Anderson et al. (2021) demonstrated distinct regions of bias in NO_2 related to biomass
326 burning and lightning emissions. Modeled HCHO, on the other hand, is not correlated with observations
327 and is biased low by -77%. Modeled water vapor layers are all modestly correlated with observations (r^2
328 of 0.64 or greater) but vary in their bias, with the 925, 850, 700, and 300 hPa layers biased within 30%
329 and the remaining layers biased up to 71%.

330
331 The satellite product is insensitive to the differences between the HCHO distribution of the satellite and
332 training dataset highlighted in Figure 1. To determine the effects of the difference in HCHO distribution,
333 we extended the training dataset to cover the full time period of the MERRA2 GMI simulation (1980 –
334 2019) and then subsampled the resultant data to match the satellite HCHO distribution. Extending the
335 training dataset to 1980 allows for the subsampled training dataset to have a similar size (~600,000
336 points) as the original training set. We then created a new machine learning model using this sub-
337 sampled dataset and calculated OH fields for Feb. 2017 using the satellite inputs from Table 1. We
338 compared this to the TCOH field calculated from a model using the original training dataset, finding
339 agreement within 5%. Similarly, the satellite-constrained TCOH product discussed in Section 4.2 differs
340 by only 3% on average from one determined with a GBRT model that excludes HCHO as an input,
341 suggesting the limited impact of potential errors in the MERRA2 GMI HCHO distribution on model
342 performance. These uncertainties are small in comparison to that resulting from uncertainties in the
343 NO_2 and HCHO satellite retrievals discussed in Section 5.2. If the uncertainty of the satellite inputs
344 decreases, as retrievals and instruments improve, then it will become necessary to more closely align
345 the training and observed HCHO distributions.

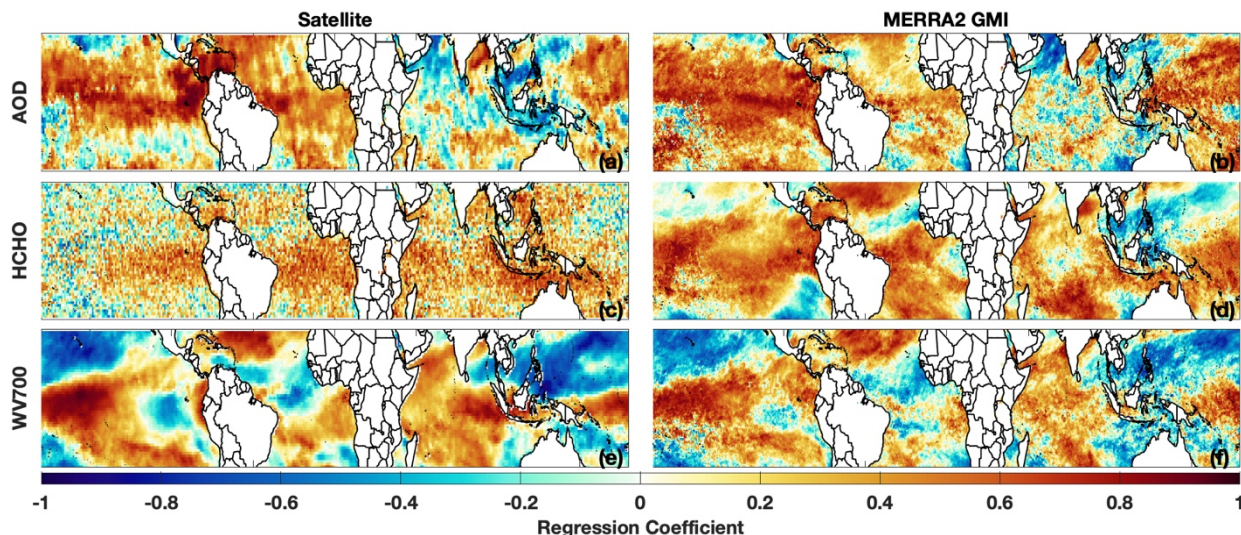
346
347 Finally, because NO_2 and HCHO have the largest differences between satellite observations and the
348 training dataset, we trained a separate machine learning model to predict TCOH, omitting these two

349 species as inputs. When this model was evaluated using the independent MERRA2 GMI output
 350 described in Section 4.1, the NRMSE was 10.1%, a more than factor of 2 degradation in performance as
 351 compared to the baseline model. This suggests that omitting these species from the machine learning
 352 model would result in a greater uncertainty in the final TCOH product than that which results from the
 353 retrieval uncertainties and the potential discrepancies between observations and the training dataset.
 354

355 3.2 Evaluation of the simulated ENSO-related variability of OH drivers

356 Because ENSO is the dominant mode of OH variability (Anderson et al., 2021; Turner et al., 2018), the
 357 training dataset must also capture the ENSO-related variability of the GBRT model inputs. Anderson et
 358 al. (2021) demonstrated that the correlation of columns of CO, H₂O_(v), and to a lesser extent NO₂, from
 359 the MERRA2 GMI simulation with the Multivariate ENSO Index (MEI) (Wolter and Timlin, 2011) agreed
 360 closely with correlations of the corresponding species for observations from MOPITT, AIRS, and OMI.
 361 Unsurprisingly, based on the strong correlation and low bias of MERRA2 GMI SSTs with observations, the
 362 simulation also captures the relationship between SSTs and ENSO. The simulation therefore sufficiently
 363 captures the ENSO-related variability of these species to act as training data for the GBRT model. We
 364 now evaluate this relationship for the remaining GBRT model inputs.
 365

366 The MERRA2 GMI-simulated ENSO-related variability of AOD and the various water vapor layers also
 367 agrees well with observations. Figures 2 and S4 show the correlation of AOD, HCHO, and the various
 368 H₂O_(v) layers with the MEI for the satellite retrievals and MERRA2 GMI. MERRA2 GMI captures the
 369 general distribution and magnitude of correlation between AOD and ENSO, despite the low optical
 370 depths over much of the domain. There are some regional differences, however, particularly in the
 371 eastern Southern Hemispheric Pacific. For the H₂O_(v) layers, the simulation underestimates the
 372 magnitude of the correlation in some areas, but in general, there is excellent agreement for all layers
 373 throughout the troposphere. This suggests that, despite the high bias discussed above, including the
 374 H₂O_(v) layers could provide important, vertically-resolved information to the machine learning model.
 375



376
 377 **Figure 2:** Distribution of the regression coefficient of a linear least squares fit of the indicated variable against the
 378 MEI for the respective satellite retrieval (a, c, and e) and MERRA2 GMI (b,d, and f) for February. Regressions of
 379 AOD are for 2010 to 2019, the years for which we have a one-degree, gridded satellite product, while HCHO and

380 water vapor 700 hPa are for 2005 to 2019. Satellite data are on a $1^\circ \times 1^\circ$ grid while model output is at the native
381 model resolution.

382 Modeled accuracy of the HCHO-ENSO relationship is more difficult to assess. While both the OMI
383 retrieval and MERRA2 GMI demonstrate broad regions of anti-correlation between HCHO and ENSO, the
384 correlations with OMI HCHO are weaker and noisier than for the other satellite retrievals. Over much of
385 the domain, HCHO abundance is low, often at or below the retrieval detection limit, suggesting that the
386 HCHO retrieval might not be of sufficient quality to capture ENSO-related variability. We investigate the
387 impacts of the HCHO observational uncertainty in Section 5.
388

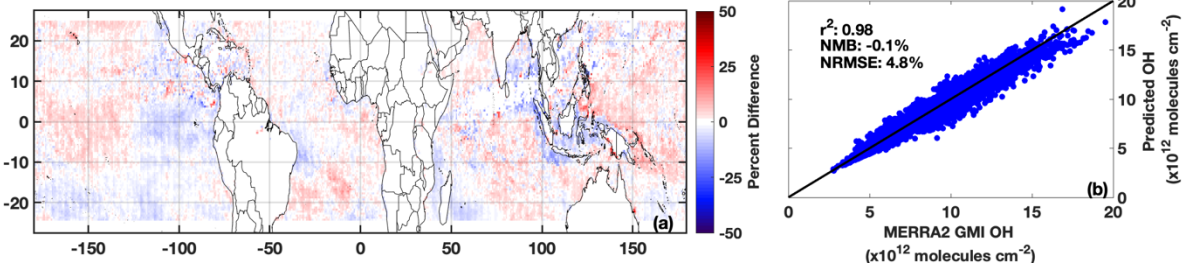
389 Finally, because we use total column O_3 as an input to the GBRT model, we do not evaluate the
390 relationship between ENSO and O_3 , as the stratosphere dominates the O_3 column and the ENSO-related
391 variability is mostly confined to the troposphere. Oman et al. (2013) found that a GEOS CCM simulation
392 and a combination of O_3 retrievals from the Microwave Limb Sounder (MLS) and the Tropospheric
393 Emission Spectrometer (TES) exhibited similar ENSO-related variability in the middle and upper
394 troposphere, demonstrating that simulations in the GEOS framework can capture this relationship. If a
395 TES-like satellite retrieval were currently available, it could be a valuable contributor to the GBRT model
396 described here, as it would provide vertically-resolved information about one of the primary drivers of
397 OH production.
398

399 4 Tropical tropospheric column OH constrained with observations of its drivers

400 We now demonstrate the ability of the GBRT model to determine TCOH. First, we show that the GBRT
401 model can reproduce MERRA2 GMI modeled TCOH from a year independent of the training dataset, a
402 so-called “hold out set” (Sect. 4.1). We then input satellite data from one month from each season into
403 the GBRT model to evaluate the realism of the calculated TCOH fields (Sect 4.2).
404

405 4.1 Evaluation with an independent year from MERRA2 GMI

406 The machine learning model is able to capture both the magnitude and the variability of TCOH across
407 each season when applied to MERRA2 GMI output from 2017, a year independent of the training
408 dataset. For August 2017 (Fig. 3b), the predicted TCOH is highly correlated with MERRA2 GMI (r^2 of
409 0.98). TCOH from the machine learning model agrees with the CTM simulation within 4.8% on average.
410 The overall normalized mean bias (NMB) is negligible (-0.1%), although there are some regions of
411 coherent bias (Fig. 3a). Results are similar for February, May, and October 2017 (Fig. S5). The
412 normalized root mean square error for each of these months is comparable to that found for a GBRT
413 parameterization of OH created with a similar methodology that included 27 inputs (Anderson et al.,
414 2022). This suggests that limiting inputs to model variables observable from space does not degrade the
415 ability of the machine learning model to predict TCOH. The low bias and high correlation between the
416 GBRT and MERRA2 GMI TCOH for all four months examined here also suggests that any potential
417 overfitting by the GBRT model is minimal.



418
419 **Figure 3:** Percent difference between TCOH predicted by the machine learning model and that from MERRA2 GMI
420 for August 2017, a month and year omitted from the training dataset (a). A regression of the machine learning TCOH

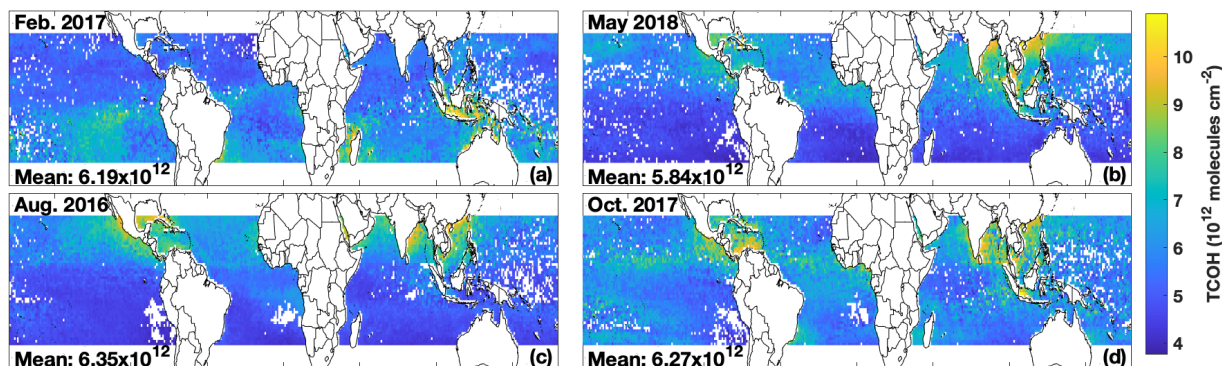
421 against MERRA2 GMI for the same month (b). The r^2 of a linear, least squares regression, along with the normalized
422 mean bias (NMB) and normalized root mean square error (NRMSE), are also indicated.

423 4.2 TCOH from satellite observations of its drivers

424 We now apply satellite data from the four months corresponding to the ATom campaign (Aug. 2016,
425 Feb. 2017, Oct. 2017, and May 2018) to the GBRT model to determine TCOH fields across the tropics.
426 More details about ATom as well as evaluation of the GBRT model with ATom observations are in
427 Section 5. We use the satellite observations listed in Table 1, all of which have been averaged to the
428 monthly scale and to a $1^\circ \times 1^\circ$ horizontal resolution. We include only grid boxes with observations for
429 all GBRT model inputs and where those observations are within the range of the corresponding inputs
430 from the training dataset. Because the satellite inputs for most species exclude grid boxes with a cloud
431 fraction greater than approximately 30%, the product presented here represents predominantly clear
432 sky conditions.

433
434 The GBRT model and multi-satellite inputs yield TCOH fields that are geophysically credible based on our
435 current understanding of OH photochemistry. Although the domain-wide average changes little with
436 season, with a minimum of 5.84×10^{12} molecules/cm² in May 2018 and a maximum of 6.35×10^{12}
437 molecules/cm² in August 2016, the spatial distribution varies widely among the four months (Fig. 4). In
438 both Feb. 2017 and Aug. 2016, TCOH minimizes in the winter hemisphere, consistent with lower OH
439 production due to low insolation. The reverse is true for the summer hemisphere. In addition, TCOH
440 maximizes in regions with strong continental outflow and along coastlines, regions likely to be impacted
441 by anthropogenic and biomass burning emissions of OH drivers.

442



443
444 **Figure 4:** TCOH calculated with the machine learning model using satellite inputs for the months of each ATom
445 deployment: Feb. 2017 (a), May 2018 (b), Aug. 2016 (c), and Oct. 2017 (d). The mean, domain-wide TCOH value in
446 molecules/cm² for each month is also indicated.

447 In general, TCOH from the multi-satellite product differs in both magnitude and distribution from the
448 MERRA2 GMI simulation. For example, for Feb. 2017, mean MERRA2 GMI TCOH is 6.96×10^{12}
449 molecules/cm², 12% higher than the satellite product (Fig. S6). This is consistent with the comparison to
450 *in situ* observations discussed in Section 3.1 where MERRA2 GMI overestimates ATom observations by
451 ~20% and underestimates CH₄ lifetime, suggesting that the satellite product is again of reasonable
452 magnitude. While understanding the satellite/model differences in TCOH is beyond the scope of this
453 work, we consider the variety in TCOH spatial distributions generated by the GBRT model to be
454 promising. The difference between the satellite-constrained product and MERRA2 GMI lends some
455 confidence that the GBRT model is not overfit or “tied” to geographic determiners in the training
456 dataset, but rather, is sensitive to variations in the chemical and dynamical drivers of OH. These results
457 all suggest that the methodology presented here can produce a reasonable satellite TCOH product in the

458 tropics, with values and distributions independent of the chemistry model used to create the GBRT
459 model.

460

461 **5 Understanding and mitigating potential challenges in using this methodology to constrain TCOH**

462 In this section, we outline possible limitations of the machine learning methodology and the current
463 observational network of the GBRT model inputs and provide potential means to mitigate these
464 limitations where necessary. In section 5.1, we discuss the current lack of sufficient in situ observations
465 to thoroughly evaluate the methodology, highlighting this point by validating the GBRT model with data
466 from the ATom campaign. In section 5.2, we investigate the impacts of random retrieval errors in
467 satellite retrievals on the TCOH product, while in section 5.3, we evaluate the impacts on TCOH when
468 using different satellite retrievals as inputs.

469

470 **5.1 Insufficient in situ observations for thorough independent evaluation**

471 While we demonstrated in Section 4.1 that TCOH calculated with the GBRT model agrees closely with a
472 hold-out set from MERRA2 GMI, it is also important to demonstrate that the GBRT model can replicate
473 observed TCOH from the actual atmosphere. Because the satellite TCOH product shown in Figure 4 is
474 monthly and at a $1^\circ \times 1^\circ$ resolution, however, there are no observations with which to evaluate the
475 product. We can test the ability of the GBRT model to reproduce observed TCOH from field campaigns,
476 however, assuming there are concomitant observations of the input species listed in Table 1. The
477 additional need for tropospheric column values of many of these species severely limits the datasets
478 available for validation. To our knowledge, the ATom campaign is the only source of the required inputs
479 with enough observations to attempt a limited validation.

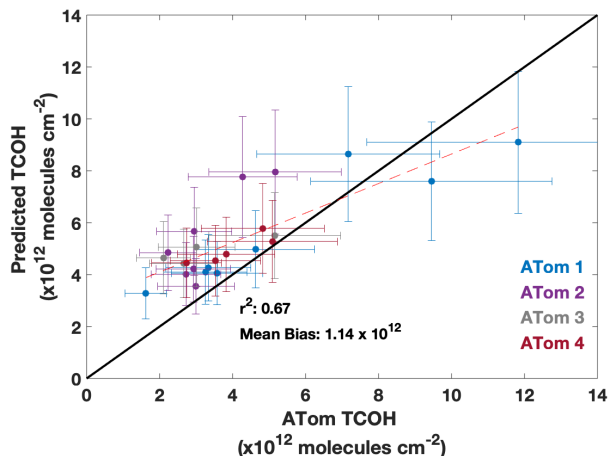
480

481 During ATom (Thompson et al., 2022), scientists measured a suite of air quality and climate relevant
482 trace gases and aerosols throughout the atmosphere above the remote Pacific and Atlantic. ATom took
483 place in four parts: ATom 1 (July – August 2016), ATom 2 (January – February 2017), ATom 3 (September
484 – October 2017), and ATom 4 (April – May 2018). During each deployment, flights consisted of a series
485 of ascents and descents across all tropical latitudes over the Pacific and Atlantic Oceans. This allows for
486 the calculation of tropospheric column content of the observed species and evaluation of the machine
487 learning model across most latitudes of our study domain and across all seasons.

488

489 To evaluate the GBRT model performance, we calculated TCOH using a modified GBRT model and
490 observations from the ATom deployments as inputs. We then compared the values to the observed OH
491 columns. To calculate the column values from the observations, we averaged data into 25 hPa pressure
492 bins for each ATom profile. We filled in missing data using a log-linear interpolation and then integrated
493 the column. Our analysis here includes only profiles with observations of all necessary species, that
494 spanned at least 700 hPa, and where less than 25% of the pressure bin values were interpolated. We
495 also omitted any profiles that had pressure bins with negative OH values. In addition, we restrict our
496 analysis to latitudes within 25° of the equator and profiles conducted between 12:00 and 15:00 LST.
497 Values for total column O_3 , AOD, and SSTs, for which there were no observations during ATom, were
498 taken from the MERRA2 GMI simulation from the grid box closest to the center of the respective profile.
499 Because ATom profiles did not span the entire tropospheric column, we trained a separate GBRT model
500 where OH and all tropospheric column input variables were substituted with columns spanning 990 –
501 250 hPa, the median range of ATom profiles. This allows for a more direct comparison between
502 observed and modeled TCOH. The spatial distribution of the valid ATom columns and the corresponding
503 columns calculated with the GBRT model are shown in Figure S7.

504



505
 506 **Figure 5:** Regression of TCOH observed from the ATom deployments against that predicted from the GBRT model.
 507 Error bars represent the 2σ observational uncertainty as reported in Brune et al. (2020) and the GBRT uncertainty
 508 described in Section 5.2. The r^2 of a linear least squares fit and the mean bias are also shown.

509 The GBRT model captures the variability of the observed TCOH, and, while there is a modest overall high
 510 bias, the median normalized absolute error of 28.3% is within observational uncertainty. When applied
 511 to all ATom deployments, predicted TCOH is correlated with the observations with an r^2 of 0.67 and a
 512 mean bias of 1.14×10^{12} molecules/cm² (Fig.5). Many of the data points agree within the combined
 513 modeled and observational uncertainty. The r^2 values for individual deployments are 0.88 for ATom 1,
 514 0.73 for ATom2, and 0.78 for ATom 3 and 4. The level of agreement between observed and predicted
 515 OH is comparable or better than that of other methods to infer OH from space. For example, Pimlott et
 516 al. (2022) found an r of 0.78 ($r^2 = 0.61$) when estimating ATom OH using a steady state approach, with r
 517 values ranging from 0.51 to 0.85 (r^2 of 0.26 to 0.72) for the different deployments. The level of
 518 agreement we show here therefore demonstrates the validity of the machine learning method to
 519 capture the variability of OH.

520
 521 The source of the model/measurement disagreement, with over- and underprediction at low and high
 522 column content respectively, is unclear, although there are multiple potential error sources. For
 523 example, a typical profile taken during ATom spanned 300 – 400 km in latitude, disconnecting the top
 524 and bottom of the profile in space. This is in contrast to the data used to train the model, which were
 525 vertical columns over one location. This could lead to a degradation in model performance when
 526 applied to ATom, since the columns are not directly analogous to the training dataset. These effects are
 527 likely limited because ATom observations are in the remote atmosphere, where the spatial distribution
 528 of relevant species is likely to be more homogeneous than over land.

529
 530 Further, there is a known interference with the ATom NO₂ observations, suggesting another possible
 531 contributor to disagreement between measured and modeled OH. Because of thermal degradation of
 532 NO₂ reservoir species, such as organic nitrates and peroxyacetyl nitrate, in the instrument inlet, ATom
 533 NO₂ observations are likely biased high (Silvern et al., 2018; Shah et al., 2023; Nault et al., 2015). To test
 534 the potential impact of NO₂ on the predicted OH columns, we applied the ATom observations to a model
 535 that omits NO₂ as an input. Removing NO₂ increases the r^2 to 0.74, decreases the mean bias to $0.82 \times$
 536 10^{12} molecules/cm², and decreases the median normalized absolute error slightly to 25.7% (Fig. S8).
 537 These improvements in performance suggest that errors in NO₂ could be contributing to the
 538 measurement/model differences. Omitting NO₂ does, however, likely introduce additional errors as NO_x
 539 compounds are essential to OH production in some regions of the atmosphere. When we apply the hold

540 out set from MERRA2 GMI to this model, for example, the NRMSE increases by approximately 50%,
541 highlighting the importance of keeping NO₂ as an input variable.

542
543 For more certain evaluation of the GBRT model with observations, greater certainty in the in situ NO₂
544 observations is needed. Although the in situ observations are insufficient to evaluate the absolute
545 accuracy of the product, the results presented here demonstrate that a machine learning model trained
546 on data from a CTM simulation can capture TCOH variability in the actual atmosphere and suggest that
547 predicted OH columns agree with observations within instrumental uncertainty.

548 549 **5.2 Impacts of uncertainties in the satellite retrievals on TCOH**

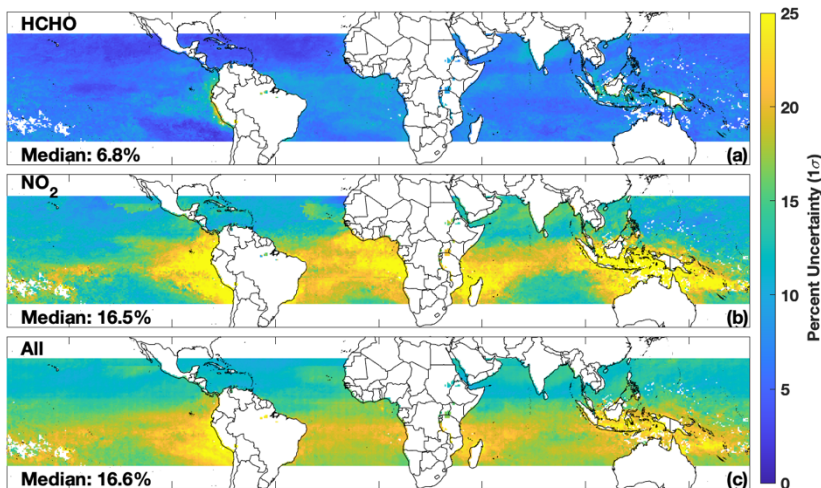
550 In the remote atmosphere where HCHO and NO₂ abundances are low, retrieval uncertainty of an
551 individual pixel for both species can be on the order of 100% and is often reflective of the *a priori*
552 (González Abad et al., 2015; Lamsal et al., 2021). Given the importance of these species to the GBRT
553 model as well as to OH chemistry, it is necessary to determine how the propagation of the retrieval
554 uncertainties from these and other model inputs impacts the predicted TCOH.

555
556 We determined the total uncertainty in TCOH from all inputs as well as the resultant uncertainty from
557 each individual input for Feb. 2017. First, we estimated an average retrieval uncertainty for each input
558 based on reported values in the retrieval files or from the literature (Table S1). We note that for NO₂
559 and HCHO we use a fit uncertainty for a single retrieval. Because we are using monthly-averaged data at
560 1° × 1° horizontal resolution, this likely significantly overestimates the actual uncertainty in these
561 retrievals as the random error from individual pixels will tend to cancel when averaged over such large
562 spatial and temporal scales. Our results are therefore an upper bound on the estimated TCOH
563 uncertainty.

564
565 Next, for each grid box and model input, we created a Gaussian distribution of 2000 values with the
566 modeled value for Feb. 2017 as the mean and the estimated uncertainty as the standard deviation. For
567 each input, we then ran the GBRT model 2000 times to create a distribution of predicted TCOH values
568 for each grid box. The normalized uncertainty in TCOH attributable to a given input is the ratio of the
569 standard deviation of the resultant distribution divided by the mean value. We repeated this process
570 individually for all inputs. In addition, to estimate a total uncertainty in TCOH, we varied all inputs
571 simultaneously with the same Gaussian distributions described above.

572
573 Uncertainty from the NO₂ retrieval, and to a lesser extent HCHO, dominates the total uncertainty in the
574 TCOH product but is of a magnitude comparable to that of in situ OH observations. Median TCOH 1σ
575 uncertainty resulting from NO₂ is 16.5%, with maxima in the remote atmosphere in regions where NO₂
576 columns are low. Median uncertainty in TCOH resulting from HCHO is 7%, averaged over the study
577 domain, despite the large uncertainty in the HCHO retrieval itself. In contrast to NO₂, uncertainties in
578 TCOH resulting from HCHO maximize in regions with higher HCHO columns (Fig. 6). The magnitude of
579 that uncertainty is likely an overestimate as the actual retrieval uncertainty for HCHO in these regions is
580 significantly lower than the value assumed for the error analysis. In comparison, median TCOH
581 uncertainties resulting from other inputs are 2.9% or less (Figs. S9 and S10). Total TCOH uncertainty is
582 16.6% and is dominated by the NO₂ uncertainty. This uncertainty analysis is in general agreement with
583 the model feature importance (Supplementary Fig. 11), a measure of the relative importance of GBRT
584 model inputs, where HCHO and NO₂ consistently have the largest values of the satellite inputs.

585



586 **Figure 6:** Normalized 1σ uncertainty in the satellite TCOH product due to uncertainties in the HCHO (a) and NO₂ (b) retrievals. The combined uncertainty from all input species is shown in panel c.
587
588

589 These results demonstrate that the satellite retrieval inputs to the machine learning model are of
590 sufficient quality to produce a meaningful TCOH data product when averaged over large spatial and
591 temporal scales. The 2σ uncertainty in TCOH resulting from the uncertainties in these retrievals is on
592 the order of that reported for in situ OH observations (Brune et al., 2020). As discussed earlier, this is
593 also likely an upper bound on the uncertainty from random retrieval errors, and uncertainties could be
594 reduced through further averaging, although at the expense of reduced spatial and temporal resolution.
595 Improving the satellite retrievals of NO₂ and HCHO in the remote atmosphere, using retrievals with less
596 noise over the remote atmosphere such as HCHO from OMPS (González Abad et al., 2016), or
597 incorporating data from satellites with higher resolution, such as TROPOMI, could also reduce the
598 uncertainty in their retrievals and thus in TCOH. As discussed in the next section, however, systematic
599 biases between satellite retrievals can also lead to uncertainties in the TCOH.

600 601 **5.3 Sensitivity of TCOH to different satellite retrievals of GBRT inputs**

602 The satellite retrievals listed in Table 1 provide the benefit of a long record, with data from most
603 retrievals available from at least 2005 to the present. Such a rich dataset would allow for long-term
604 trend analysis of TCOH. These instruments are near the end of their life cycle, however, so it is
605 instructive to see how retrievals from newer satellites impact the predicted TCOH from the GBRT model.
606 In addition, although these newer satellites, such as TROPOMI, have a significantly shorter observational
607 record than those in Table 1, TROPOMI also has finer spatial resolution and the added advantage of
608 providing retrievals for CO, NO₂, O₃, HCHO, and H₂O_(v). Using retrievals of multiple species from the
609 same instrument could negate errors resulting from differences in viewing geometry as well as from
610 overpass time. Here, we investigate the effects of applying retrievals from TROPOMI to the machine
611 learning model and compare them to the results from the product described in Section 4, highlighting
612 potential impacts resulting from instrumental differences as well as those resulting from differences in
613 retrieval algorithms. The results emphasize the need for thorough retrieval validation in the remote
614 atmosphere, particularly of NO₂.

615 616 **5.3.1 Description of TROPOMI and a modified GBRT model**

617 TROPOMI, a successor instrument to OMI, is a spectrometer covering portions of the ultraviolet, visible,
618 and infrared spectrum (Veefkind et al., 2012). It is located onboard the Sentinel 5 Precursor satellite,
619 which is polar orbiting and has a local overpass time of approximately 13:30. Horizontal resolution for

620 the month examined here (May 2018) is as high as $7 \text{ km} \times 3.5 \text{ km}$ at nadir. We have gridded the Level 2
621 product for each species to a $1^\circ \times 1^\circ$ resolution and averaged the data to the monthly scale, applying the
622 recommended quality flags and filtering for cloud fraction greater than 30%.

623
624 We use two different retrievals of TROPOMI NO_2 for this analysis. First, we use the KNMI (Royal
625 Netherlands Meteorological Institute) NO_2 retrieval (van Geffen et al., 2020), which is based on the
626 DOMINO (Dutch OMI NO_2 product) retrieval developed for the OMI instrument. Wang et al. (2020)
627 found that this retrieval was biased high when compared to ship-based observations from a MAX-DOAS
628 instrument over the remote oceans, while Verhoelst et al. (2021) found good agreement between the
629 retrieval and ground-based observations in Reunion. In addition, we use the MINDS (Multi-Decadal
630 Nitrogen Dioxide and Derived Products from Satellites) retrieval, which uses the same algorithm as for
631 the OMI product described in Section 2 (Lamsal et al., 2022). This retrieval has not been evaluated in
632 the remote tropics.

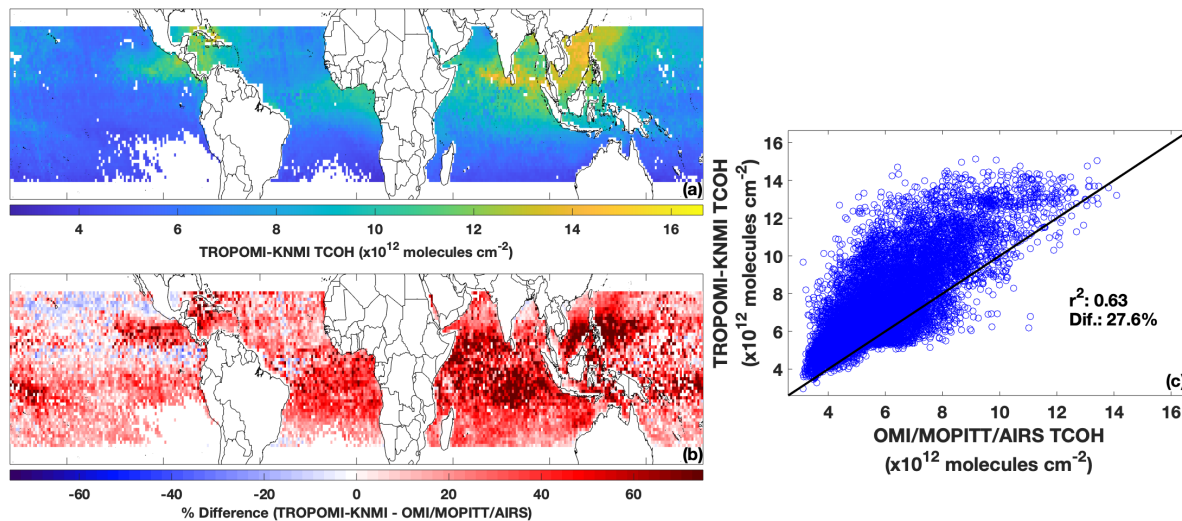
633
634 We also use TROPOMI retrievals of HCHO, $\text{H}_2\text{O}_{(\text{v})}$ column, total column O_3 , and CO. The HCHO retrieval
635 (De Smedt et al., 2018) was found to have a 30% low bias with respect to an OMI retrieval using the
636 same algorithm due to differences in cloud processing (De Smedt et al., 2021). While evaluation in the
637 remote tropics is limited, the TROPOMI retrieval does overestimate HCHO in polluted regions (De Smedt
638 et al., 2021) when compared to ground-based observations. The TROPOMI $\text{H}_2\text{O}_{(\text{v})}$ (Chan et al., 2022)
639 retrieval has a slight dry bias with comparison to other satellite products, while the total column O_3
640 retrieval (Garane et al., 2019) agrees within 0 – 1.5% with ground-based observations. Finally, the CO
641 retrieval (Borsdorff et al., 2019) agrees with MOPITT over the oceans within 3% on average (Martínez-
642 Alonso et al., 2020). TROPOMI does not have an equivalent retrieval of the AIRS $\text{H}_2\text{O}_{(\text{v})}$ layers.

643
644 To calculate TCOH using TROPOMI data, we trained a separate machine learning model using all inputs
645 from Table 1 except the water vapor layers, for which there are no TROPOMI retrievals. Removal of the
646 layers from the machine learning model does not significantly degrade performance. For example, for
647 May 2017, removing the $\text{H}_2\text{O}_{(\text{v})}$ layers from the model, increases the NRMSE from 5.34% to 5.73% when
648 applying the GBRT model to the hold out set. For this new model, we then calculate TCOH using
649 TROPOMI data, including the KNMI NO_2 retrieval. For SSTs and AOD, we use the MUR and MODIS
650 products respectively. While TROPOMI does have an aerosol product, the UV aerosol index, the
651 corresponding output from the MERRA2 GMI simulation is unavailable. We refer to this TCOH as the
652 TROPOMI-KNMI product. We have also calculated TCOH using the satellite retrievals in Table 1, except
653 for the water vapor layers, using this GBRT model, and refer to that as the OMI/MOPITT/AIRS product.
654 We restrict our analysis to May 2018, the only month for which we have TROPOMI water vapor data.

655
656 **5.3.2 TROPOMI data applied to the GBRT model**
657 TCOH from the TROPOMI-KNMI product is higher than that from the OMI/MOPITT/AIRS product for May
658 2018. Figure 7 shows TCOH calculated from the TROPOMI-KNMI product as well as the percent
659 difference between the two products. While there is modest correlation between the two ($r^2 = 0.63$),
660 the TROPOMI product is 27.6% higher than the OMI/MOPITT/AIRS product, with higher values across
661 almost the entire domain. Differences between the products are most pronounced in the Indian Ocean
662 and off the coasts of Indonesia and the Philippines.

663
664 In general, observations from TROPOMI agree with those from the satellites in Table 1, with the
665 exception of NO_2 and HCHO. Ozone, $\text{H}_2\text{O}_{(\text{v})}$, and CO from TROPOMI are highly correlated (r^2 of 0.85 or
666 higher) and agree within 10% on average (Fig. S12) with their respective retrievals from OMI, MOPITT,
667 and AIRS. On the other hand, TROPOMI KNMI- NO_2 is systematically higher (145% on average), and

668 TROPOMI HCHO is 20% lower than their corresponding OMI retrievals. The higher TCOH from the
 669 TROPOMI product is consistent with the increase in NO₂, which would lead to higher secondary
 670 production of OH. Further, while TROPOMI KNMI-NO₂ is modestly correlated with OMI NO₂ ($r^2 = 0.61$),
 671 TROPOMI and OMI HCHO are not correlated ($r^2 = 0.23$), highlighting the difficulty of the HCHO retrieval.
 672 Note that we are not seeking to determine which retrieval, if any, is more accurate. We are highlighting
 673 the differences to emphasize the impact that systematic differences in retrieval magnitudes of GBRT
 674 model inputs can have on the resultant TCOH.
 675



676
 677 **Figure 7:** TCOH for May 2018 determined using TROPOMI inputs, including the KNMI NO₂ retrieval (a). The
 678 difference between the TROPOMI and multi-satellite product is shown in (b). Panel (c) shows the regression of
 679 TCOH calculated from TROPOMI against that calculated from retrievals from MOPITT, OMI, and AIRS as well as the
 680 percent difference between the two TCOH products.

681 NO₂ drives the differences between the two TCOH products. To determine the impacts of the different
 682 TROPOMI inputs on the TCOH product, we individually swapped each TROPOMI input into the
 683 OMI/MOPITT/AIRS product, replacing the corresponding input from Table 1. We then determined the
 684 difference in TCOH from the OMI/MOPITT/AIRS product that does not include TROPOMI. While this
 685 method will not yield the exact contribution from a particular retrieval because of the non-linear nature
 686 of OH chemistry, it does yield information about the relative importance of each species. Swapping in
 687 TROPOMI CO, H₂O_(v), and O₃ changed TCOH by less than 2%, while using TROPOMI HCHO increased
 688 TCOH by 3%. In contrast, TROPOMI NO₂ increased TCOH by 29%, showing that the higher TCOH in the
 689 TROPOMI product is driven by differences in NO₂.

690
 691 The increased TCOH in the TROPOMI product likely results from a combination of differences in the NO₂
 692 retrieval algorithm as well as instrumental differences. Comparison of the KNMI and MINDS retrievals
 693 illustrate this point. When compared to OMI, the MINDS NO₂ retrieval is 58% higher for May 2018, as
 694 compared to 145% higher for the KNMI retrieval. The closer agreement is unsurprising since the MINDS
 695 NO₂ uses the same retrieval algorithm as for OMI. Substituting the MINDS NO₂ as an input to the
 696 TROPOMI product (TROPOMI-MINDS product) reduces the difference with respect to the
 697 OMI/MOPITT/AIRS product to 18% (Fig. S13). While this is an improvement in agreement, the
 698 differences in TCOH as well as the lack of change in r^2 value still suggest that differences between OMI
 699 and TROPOMI unrelated to the retrieval algorithm account for some of the discrepancy. In addition, the
 700 training dataset does not take TROPOMI averaging kernels and shape factors into account, which could
 701 also contribute to the observed differences.

702
703 The results here demonstrate the sensitivity of the methodology to any systematic bias in the input
704 retrievals. As with the random error analysis, the level of uncertainty introduced by these biases is low
705 enough to allow for a meaningful OH product. Despite these differences, the methodology to determine
706 TCOH using machine learning that we have presented here still captures the variability in TCOH,
707 consistent with the ATOm evaluation outlined in Section 5.1. To reduce the uncertainty of TCOH, better
708 evaluation of NO₂ in the remote atmosphere is needed to determine which retrievals, if any, are
709 accurate.

710 711 **6 Discussion and recommendations for future observations**

712 The method of estimating clear-sky TCOH presented here has the potential to increase our
713 understanding of the atmospheric oxidation capacity. Because of the long record of observations from
714 MOPITT, OMI, AIRS, and MODIS, we can calculate tropical TCOH from 2005 to the present, and since the
715 methodology is not constrained to a particular satellite, newer satellite missions could extend the
716 dataset beyond the end of these instruments' lifetimes. In addition, this methodology will provide sub-
717 hemispheric information on OH variability, supplementing information available from MCF inversions.

718
719 The methodology could be expanded to the extra-tropics and over land, allowing for global constraints
720 on OH. Expansion over land will likely require additional satellite retrievals, like that of isoprene (Wells
721 et al., 2020), in regions with more complex VOC chemistry than in the remote atmosphere. Expanding
722 this product beyond the tropics could increase understanding of global CH₄, CO, and VOC trends and
723 variability and allow for a wider range of satellite retrievals as inputs. For example, current and
724 upcoming geostationary air quality satellites such as Sentinel 4, TEMPO (Tropospheric Emissions:
725 Monitoring of Pollution), and GEMS (Geostationary Environment Monitoring Spectrometer) could
726 provide retrievals of most of the necessary inputs to the machine learning model, allowing for the
727 understanding of diurnal variability in TCOH and potentially in the diurnal variability of ozone production
728 (Zhu et al., 2022a).

729
730 A similar methodology could likely be used to determine OH at different layers of the atmosphere.
731 Because CH₄ loss is not evenly distributed throughout the tropospheric column, vertically resolved OH
732 would better help inform this process. Vertically-resolved OH could also help understand differences in
733 OH drivers in the upper and lower troposphere (Spivakovsky et al., 1990; Lelieveld et al., 2016), which
734 can often be decoupled from the column. While column inputs, such as those discussed here, could be
735 used, the inclusion of vertically resolved satellite retrievals, such as the AIRS H₂O_(v) layers, would provide
736 additional information. Tropospheric O₃ at different atmospheric layers, such as that previously
737 provided by the TES satellite, could also be invaluable here, as O₃ is a large driver of primary OH
738 production.

739
740 Satellite-derived OH would also provide a much-needed, observational constraint on OH variability in
741 global chemistry models. Because the methodology can capture variability in TCOH of both
742 observations and 3-dimensional model output, TCOH trends from a satellite-constrained product could
743 be used to evaluate modeled trends and as well as the spatial variability resulting from events like ENSO.
744 While the satellite-derived OH could not explicitly indicate the cause of differences, the spatial
745 distribution of the differences as well as differences in observed and modeled machine learning model
746 inputs could indicate potential dynamical or emission sources of error in the 3D model.

747
748 Further, the combination of the satellite-derived OH and the machine learning model could help identify
749 the impacts of any diagnosed errors in emissions inventories as well as the impacts of unexpected

750 events, such as COVID-19-related shutdowns, on TCOH. For example, if there are significant
751 discrepancies between observed and modeled NO₂ in a specific region of the atmosphere, the satellite
752 NO₂ could be scaled to more closely match the 3D model values and then be input into the machine
753 learning model. The difference in TCOH would then indicate the relative impact of the model error. This
754 would serve as a computationally efficient complement to other methodologies constraining models
755 with observations (e.g. Miyazaki et al., 2020; Miyazaki et al., 2021) to identify the impacts of these errors
756 on the atmospheric oxidation capacity. A similar methodology could be used for unexpected events that
757 significantly impact emissions of OH drivers, allowing for quick determination of their potential impacts
758 on the atmospheric oxidation capacity before emissions inventories could be revised.

759
760 While we have shown that the methodology captures the variability of observed OH and generally
761 agrees with observations within measurement uncertainty, it is unclear whether differences result from
762 GBRT model deficiencies or structural differences between the *in situ* observations and the training
763 dataset. Additional field campaigns with observations of OH and the GBRT model inputs would allow for
764 a more thorough evaluation of both the OH product and the methodology itself. Such a field campaign
765 would need to provide complete tropospheric columns of all species and cover less horizontal distance
766 than the ATom profiles (e.g. from spiral flight patterns). In situ observations of NO₂ without significant
767 interference from NO_x reservoir species are also needed to reduce uncertainty. Alternatively, NO₂ and
768 other species could be measured through aircraft-based remote sensing. Finally, repeated sampling over
769 the same locations for multiple days within a defined area would allow for meaningful statistical analysis
770 while also allowing for the comparison of TCOH columns calculated from satellite observations.

771
772 Finally, accuracy of the TCOH product is dependent on the accuracy of the satellite retrievals input into
773 the machine learning model, with the NO₂ retrieval having the largest effect. To reduce the uncertainty
774 of the TCOH product, more information about the accuracy of individual NO₂ retrievals is required.
775 Currently, there is little validation of OMI and TROPOMI NO₂ retrievals in the remote, tropical
776 atmosphere, so it is difficult to assess which retrievals, if any, are correct. Recent efforts, such as the
777 QA4ECV (Quality Assurance for the Essential Climate Variables), to improve NO₂ retrieval algorithms
778 have reduced uncertainty, particularly over land (Boersma et al., 2018), although it is unclear how the
779 accuracy of these retrievals translates to the remote tropics as validation data are still extremely limited.
780 Even retrievals of TROPOMI and OMI made with the same algorithm show differences, suggesting that
781 instrumental differences could also affect the results. Future satellite missions should focus on trying to
782 reduce the uncertainty in NO₂ retrievals, particularly in the remote atmosphere, both through
783 improvements in instrument design and algorithm development.

784 785 **7 Data Availability**

786 Output from the MERRA2 GMI simulation are publicly available at [https://acd-
787 ext.gsfc.nasa.gov/Projects/GEOSCCM/MERRA2GMI/](https://acd-ext.gsfc.nasa.gov/Projects/GEOSCCM/MERRA2GMI/) (NASA Goddard Space Flight Center, 2023). All
788 satellite products, except for TROPOMI water vapor, are available at [https://disc.gsfc.nasa.gov \(GES
789 DISC, 2023\)](https://disc.gsfc.nasa.gov (GES DISC, 2023)). Data from the ATom campaign are located at <https://daac.ornl.gov> (Wofsy et al., 2021).

790 791 **8 Author contributions**

792 DCA wrote the manuscript, performed the data analysis, and created the GBRT model. DCA, BND, JMN,
793 and MBFC developed the idea for the methodology. SAS performed three-dimensional modeling for the
794 work. JMN provided advice on machine learning. JL helped perform data analysis. All authors helped
795 develop ideas for the analysis and contributed to the manuscript.

796 797 **9 Competing Interests**

798 BND is a member of the editorial board of Atmospheric Chemistry and Physics. The peer-review process
799 was guided by an independent editor, and the authors also have no other competing interests to
800 declare.

801

802 **10 Financial support**

803 This research has been supported by the National Aeronautics and Space Administration (NASA)
804 Atmospheric Composition Campaign Data Analysis and Modeling (ACCDAM) program (grant no.
805 80NSSC21K1440).

806

807 **11 Acknowledgements**

808 The authors wish to thank Lok Chan and Diego Loyola for use of the TROPOMI water vapor product.

809

810 **10. References**

811

812 Anderson, D. C., Nicely, J. M., Salawitch, R. J., Canty, T. P., Dickerson, R. R., Hanisco, T. F., Wolfe, G. M.,
813 Apel, E. C., Atlas, E., Bannan, T., Bauguitte, S., Blake, N. J., Bresch, J. F., Campos, T. L., Carpenter, L. J.,
814 Cohen, M. D., Evans, M., Fernandez, R. P., Kahn, B. H., Kinnison, D. E., Hall, S. R., Harris, N. R., Hornbrook,
815 R. S., Lamarque, J. F., Le Breton, M., Lee, J. D., Percival, C., Pfister, L., Pierce, R. B., Riemer, D. D., Saiz-
816 Lopez, A., Stunder, B. J., Thompson, A. M., Ullmann, K., Vaughan, A., and Weinheimer, A. J.: A pervasive
817 role for biomass burning in tropical high ozone/low water structures, *Nat Commun*, 7, 10267,
818 10.1038/ncomms10267, 2016.

819 Anderson, D. C., Duncan, B. N., Fiore, A. M., Baublitz, C. B., Follette-Cook, M. B., Nicely, J. M., and Wolfe,
820 G. M.: Spatial and temporal variability in the hydroxyl (OH) radical: understanding the role of large-scale
821 climate features and their influence on OH through its dynamical and photochemical drivers,
822 *Atmospheric Chemistry and Physics*, 21, 6481-6508, 10.5194/acp-21-6481-2021, 2021.

823 Anderson, D. C., Follette-Cook, M. B., Strode, S. A., Nicely, J. M., Liu, J., Ivatt, P. D., and Duncan, B. N.: A
824 machine learning methodology for the generation of a parameterization of the hydroxyl radical, *Geosci.*
825 *Model Dev.*, 15, 6341-6358, 10.5194/gmd-15-6341-2022, 2022.

826 Bedka, S., Knuteson, R., Revercomb, H., Tobin, D., and Turner, D.: An assessment of the absolute
827 accuracy of the Atmospheric Infrared Sounder v5 precipitable water vapor product at tropical,
828 midlatitude, and arctic ground-truth sites: September 2002 through August 2008, *Journal of Geophysical*
829 *Research: Atmospheres*, 115, D17310, <https://doi.org/10.1029/2009JD013139>, 2010.

830 Boersma, K. F., Eskes, H. J., Richter, A., De Smedt, I., Lorente, A., Beirle, S., van Geffen, J. H. G. M., Zara,
831 M., Peters, E., Van Roozendaal, M., Wagner, T., Maasakkers, J. D., van der A, R. J., Nightingale, J., De
832 Rudder, A., Irie, H., Pinardi, G., Lambert, J. C., and Compornolle, S. C.: Improving algorithms and
833 uncertainty estimates for satellite NO₂ retrievals: results from the quality assurance for the essential
834 climate variables (QA4ECV) project, *Atmos. Meas. Tech.*, 11, 6651-6678, 10.5194/amt-11-6651-2018,
835 2018.

836 Borsdorff, T., aan de Brugh, J., Schneider, A., Lorente, A., Birk, M., Wagner, G., Kivi, R., Hase, F., Feist, D.
837 G., Sussmann, R., Rettinger, M., Wunch, D., Warneke, T., and Landgraf, J.: Improving the TROPOMI CO
838 data product: update of the spectroscopic database and destriping of single orbits, *Atmos. Meas. Tech.*,
839 12, 5443-5455, 10.5194/amt-12-5443-2019, 2019.

840 Brune, W. H., Miller, D. O., Thames, A. B., Allen, H. M., Apel, E. C., Blake, D. R., Bui, T. P., Commane, R.,
841 Crouse, J. D., Daube, B. C., Diskin, G. S., DiGangi, J. P., Elkins, J. W., Hall, S. R., Hanisco, T. F., Hannun, R.
842 A., Hints, E. J., Hornbrook, R. S., Kim, M. J., McKain, K., Moore, F. L., Neuman, J. A., Nicely, J. M., Peischl,
843 J., Ryerson, T. B., St. Clair, J. M., Sweeney, C., Teng, A. P., Thompson, C., Ullmann, K., Veres, P. R.,
844 Wennberg, P. O., and Wolfe, G. M.: Exploring Oxidation in the Remote Free Troposphere: Insights From
845 Atmospheric Tomography (ATom), *Journal of Geophysical Research: Atmospheres*, 125, e1019JD031685,
846 10.1029/2019jd031685, 2020.

847 Buchholz, R. R., Deeter, M. N., Worden, H. M., Gille, J., Edwards, D. P., Hannigan, J. W., Jones, N. B.,
848 Paton-Walsh, C., Griffith, D. W. T., Smale, D., Robinson, J., Strong, K., Conway, S., Sussmann, R., Hase, F.,
849 Blumenstock, T., Mahieu, E., and Langerock, B.: Validation of MOPITT carbon monoxide using ground-
850 based Fourier transform infrared spectrometer data from NDACC, *Atmos. Meas. Tech.*, 10, 1927-1956,
851 10.5194/amt-10-1927-2017, 2017.

852 Burnett, C. R., and Minschwaner, K.: Continuing development in the regime of decreased atmospheric
853 column OH at Fritz Peak, Colorado, *Geophysical Research Letters*, 25, 1313-1316,
854 <https://doi.org/10.1029/98GL01062>, 1998.

855 Chan, K. L., Xu, J., Slijkhuis, S., Valks, P., and Loyola, D.: TROPOspheric Monitoring Instrument
856 observations of total column water vapour: Algorithm and validation, *Science of The Total Environment*,
857 821, 153232, <https://doi.org/10.1016/j.scitotenv.2022.153232>, 2022.

858 Chen, T., and Guestrin, C.: XGBoost: A Scalable Tree Boosting System, *KDD '16: Proceedings of the 22nd*
859 *ACM SIGKDD International Conference on Knowledge Discovery and Data Mining*, 13 - 17 Aug. 2016,
860 785-794, San Francisco, CA, USA, <https://doi.org/10.1145/2939672.2939785>, 2016.

861 Chin, T. M., Vazquez-Cuervo, J., and Armstrong, E. M.: A multi-scale high-resolution analysis of global sea
862 surface temperature, *Remote Sensing of Environment*, 200, 154-169,
863 <https://doi.org/10.1016/j.rse.2017.07.029>, 2017.

864 Choi, S., Lamsal, L. N., Follette-Cook, M., Joiner, J., Krotkov, N. A., Swartz, W. H., Pickering, K. E.,
865 Loughner, C. P., Appel, W., Pfister, G., Saide, P. E., Cohen, R. C., Weinheimer, A. J., and Herman, J. R.:
866 Assessment of NO₂ observations during DISCOVER-AQ and KORUS-AQ field campaigns, *Atmos. Meas.*
867 *Tech.*, 13, 2523-2546, 10.5194/amt-13-2523-2020, 2020.

868 De Smedt, I., Theys, N., Yu, H., Danckaert, T., Lerot, C., Compennolle, S., Van Roozendaal, M., Richter, A.,
869 Hilboll, A., Peters, E., Pedernana, M., Loyola, D., Beirle, S., Wagner, T., Eskes, H., van Geffen, J.,
870 Boersma, K. F., and Veefkind, P.: Algorithm theoretical baseline for formaldehyde retrievals from S5P
871 TROPOMI and from the QA4ECV project, *Atmospheric Measurement Techniques*, 11, 2395-2426,
872 10.5194/amt-11-2395-2018, 2018.

873 De Smedt, I., Pinardi, G., Vigouroux, C., Compennolle, S., Bais, A., Benavent, N., Boersma, F., Chan, K. L.,
874 Donner, S., Eichmann, K. U., Hedelt, P., Hendrick, F., Irie, H., Kumar, V., Lambert, J. C., Langerock, B.,
875 Lerot, C., Liu, C., Loyola, D., Piters, A., Richter, A., Rivera Cárdenas, C., Romahn, F., Ryan, R. G., Sinha, V.,
876 Theys, N., Vlietinck, J., Wagner, T., Wang, T., Yu, H., and Van Roozendaal, M.: Comparative assessment
877 of TROPOMI and OMI formaldehyde observations and validation against MAX-DOAS network column
878 measurements, *Atmos. Chem. Phys.*, 21, 12561-12593, 10.5194/acp-21-12561-2021, 2021.

879 Deeter, M. N., Edwards, D. P., Francis, G. L., Gille, J. C., Mao, D., Martínez-Alonso, S., Worden, H. M.,
880 Ziskin, D., and Andreae, M. O.: Radiance-based retrieval bias mitigation for the MOPITT instrument: the
881 version 8 product, *Atmospheric Measurement Techniques*, 12, 4561-4580, 10.5194/amt-12-4561-2019,
882 2019.

883 Duncan, B., Portman, D., Bey, I., and Spivakovsky, C.: Parameterization of OH for efficient computation in
884 chemical tracer models, *Journal of Geophysical Research: Atmospheres*, 105, 12259-12262,
885 10.1029/1999JD901141, 2000.

886 Duncan, B. N., Strahan, S. E., Yoshida, Y., Steenrod, S. D., and Livesey, N.: Model study of the cross-
887 tropopause transport of biomass burning pollution, *Atmos. Chem. Phys.*, 7, 3713-3736, 10.5194/acp-7-
888 3713-2007, 2007.

889 Elith, J., Leathwick, J. R., and Hastie, T.: A working guide to boosted regression trees, *J Anim Ecol*, 77,
890 802-813, 10.1111/j.1365-2656.2008.01390.x, 2008.

891 Garane, K., Koukouli, M. E., Verhoelst, T., Lerot, C., Heue, K. P., Fioletov, V., Balis, D., Bais, A., Bazureau,
892 A., Dehn, A., Goutail, F., Granville, J., Griffin, D., Hubert, D., Keppens, A., Lambert, J. C., Loyola, D.,
893 McLinden, C., Pazmino, A., Pommereau, J. P., Redondas, A., Romahn, F., Valks, P., Van Roozendael, M.,
894 Xu, J., Zehner, C., Zerefos, C., and Zimmer, W.: TROPOMI/S5P total ozone column data: global ground-
895 based validation and consistency with other satellite missions, *Atmos. Meas. Tech.*, 12, 5263-5287,
896 10.5194/amt-12-5263-2019, 2019.

897 Gelaro, R., McCarty, W., Suarez, M. J., Todling, R., Molod, A., Takacs, L., Randles, C., Darmenov, A.,
898 Bosilovich, M. G., Reichle, R., Wargan, K., Coy, L., Cullather, R., Draper, C., Akella, S., Buchard, V., Conaty,
899 A., da Silva, A., Gu, W., Kim, G. K., Koster, R., Lucchesi, R., Merkova, D., Nielsen, J. E., Partyka, G.,
900 Pawson, S., Putman, W., Rienecker, M., Schubert, S. D., Sienkiewicz, M., and Zhao, B.: The Modern-Era
901 Retrospective Analysis for Research and Applications, Version 2 (MERRA-2), *J Clim*, Volume 30, 5419-
902 5454, 10.1175/JCLI-D-16-0758.1, 2017.

903 GES DISC: Earth Science Data at NASA, available at <https://disc.gsfc.nasa.gov>, last access: 6 Mar. 2023.

904 González Abad, G., Liu, X., Chance, K., Wang, H., Kurosu, T. P., and Suleiman, R.: Updated Smithsonian
905 Astrophysical Observatory Ozone Monitoring Instrument (SAO OMI) formaldehyde retrieval,
906 *Atmospheric Measurement Techniques*, 8, 19-32, 10.5194/amt-8-19-2015, 2015.

907 González Abad, G., Vasilkov, A., Seftor, C., Liu, X., and Chance, K.: Smithsonian Astrophysical Observatory
908 Ozone Mapping and Profiler Suite (SAO OMPS) formaldehyde retrieval, *Atmospheric Measurement*
909 *Techniques*, 9, 2797-2812, 10.5194/amt-9-2797-2016, 2016.

910 Hedelius, J. K., He, T. L., Jones, D. B. A., Baier, B. C., Buchholz, R. R., De Mazière, M., Deutscher, N. M.,
911 Dubey, M. K., Feist, D. G., Griffith, D. W. T., Hase, F., Iraci, L. T., Jeseck, P., Kiel, M., Kivi, R., Liu, C.,
912 Morino, I., Notholt, J., Oh, Y. S., Ohyama, H., Pollard, D. F., Rettinger, M., Roche, S., Roehl, C. M.,
913 Schneider, M., Shiomi, K., Strong, K., Sussmann, R., Sweeney, C., Té, Y., Uchino, O., Velazco, V. A., Wang,
914 W., Warneke, T., Wennberg, P. O., Worden, H. M., and Wunch, D.: Evaluation of MOPITT Version 7 joint
915 TIR–NIR XCO retrievals with TCCON, *Atmos. Meas. Tech.*, 12, 5547-5572, 10.5194/amt-12-5547-2019,
916 2019.

917 Ivatt, P. D., and Evans, M. J.: Improving the prediction of an atmospheric chemistry transport model
918 using gradient-boosted regression trees, *Atmospheric Chemistry and Physics*, 20, 8063-8082,
919 10.5194/acp-20-8063-2020, 2020.

920 Keller, C. A., and Evans, M. J.: Application of random forest regression to the calculation of gas-phase
921 chemistry within the GEOS-Chem chemistry model v10, *Geoscientific Model Development*, 12, 1209-
922 1225, 10.5194/gmd-12-1209-2019, 2019.

923 Kelp, M. M., Jacob, D. J., Kutz, J. N., Marshall, J. D., and Tessum, C. W.: Toward Stable, General Machine-
924 Learned Models of the Atmospheric Chemical System, *Journal of Geophysical Research: Atmospheres*,
925 125, e2020JD032759, <https://doi.org/10.1029/2020JD032759>, 2020.

926 Labow, G. J., McPeters, R. D., Bhartia, P. K., and Kramarova, N.: A comparison of 40 years of SBUV
927 measurements of column ozone with data from the Dobson/Brewer network, *Journal of Geophysical*
928 *Research: Atmospheres*, 118, 7370-7378, <https://doi.org/10.1002/jgrd.50503>, 2013.

929 Lamsal, L. N., Krotkov, N. A., Celarier, E. A., Swartz, W. H., Pickering, K. E., Bucsela, E. J., Gleason, J. F.,
930 Martin, R. V., Philip, S., Irie, H., Cede, A., Herman, J., Weinheimer, A., Szykman, J. J., and Knepp, T. N.:
931 Evaluation of OMI operational standard NO₂ column retrievals using in situ and surface-based NO₂
932 observations, *Atmospheric Chemistry and Physics*, 14, 11587-11609, 10.5194/acp-14-11587-2014, 2014.

933 Lamsal, L. N., Krotkov, N. A., Vasilkov, A., Marchenko, S., Qin, W., Yang, E. S., Fasnacht, Z., Joiner, J., Choi,
934 S., Haffner, D., Swartz, W. H., Fisher, B., and Bucsela, E.: Ozone Monitoring Instrument (OMI) Aura
935 nitrogen dioxide standard product version 4.0 with improved surface and cloud treatments, *Atmos.*
936 *Meas. Tech.*, 14, 455-479, 10.5194/amt-14-455-2021, 2021.

937 Lamsal, L. N., Krotkov, N. A., Marchenko, S. V., Joiner, J., Oman, L., Vasilkov, A., Fisher, B., Qin, W., Yang,
938 E.-S., Fasnacht, Z., Choi, S., Leonard, P., and Haffner, D.: TROPOMI/S5P NO₂ Tropospheric, Stratospheric
939 and Total Columns MINDS 1-Orbit L2 Swath 5.5 km x 3.5 km, in, *NASA Goddard Earth Sciences Data and*
940 *Information Services Center (GES DISC) [data set]*, <https://10.5067/MEASURES/MINDS/Data203>, 2022.

941 Laughner, J. L., Neu, J. L., Schimel, D., Wennberg, P. O., Barsanti, K., Bowman, K. W., Chatterjee, A.,
942 Croes, B. E., Fitzmaurice, H. L., Henze, D. K., Kim, J., Kort, E. A., Liu, Z., Miyazaki, K., Turner, A. J.,
943 Anenberg, S., Avise, J., Cao, H., Crisp, D., de Gouw, J., Eldering, A., Fyfe, J. C., Goldberg, D. L., Gurney, K.
944 R., Hasheminassab, S., Hopkins, F., Ivey, C. E., Jones, D. B. A., Liu, J., Lovenduski, N. S., Martin, R. V.,
945 McKinley, G. A., Ott, L., Poulter, B., Ru, M., Sander, S. P., Swart, N., Yung, Y. L., and Zeng, Z. C.: Societal
946 shifts due to COVID-19 reveal large-scale complexities and feedbacks between atmospheric chemistry
947 and climate change, *Proc Natl Acad Sci U S A*, 118, e2109481118, 10.1073/pnas.2109481118, 2021.

948 Lelieveld, J., Gromov, S., Pozzer, A., and Taraborrelli, D.: Global tropospheric hydroxyl distribution,
949 budget and reactivity, *Atmos. Chem. Phys.*, 16, 12477-12493, 10.5194/acp-16-12477-2016, 2016.

950 Levy, R. C., Mattoo, S., Munchak, L. A., Remer, L. A., Sayer, A. M., Patadia, F., and Hsu, N. C.: The
951 Collection 6 MODIS aerosol products over land and ocean, *Atmos. Meas. Tech.*, 6, 2989-3034,
952 10.5194/amt-6-2989-2013, 2013.

953 Liang, Q., Chipperfield, M. P., Fleming, E. L., Abraham, N. L., Braesicke, P., Burkholder, J. B., Daniel, J. S.,
954 Dhomse, S., Fraser, P. J., Hardiman, S. C., Jackman, C. H., Kinnison, D. E., Krummel, P. B., Montzka, S. A.,
955 Morgenstern, O., McCulloch, A., Mühle, J., Newman, P. A., Orkin, V. L., Pitari, G., Prinn, R. G., Rigby, M.,

956 Rozanov, E., Stenke, A., Tummon, F., Velders, G. J. M., Visioni, D., and Weiss, R. F.: Deriving Global OH
957 Abundance and Atmospheric Lifetimes for Long-Lived Gases: A Search for CH₃CCl₃ Alternatives, *Journal*
958 *of Geophysical Research: Atmospheres*, 122, 11,914-911,933, 10.1002/2017JD026926, 2017.

959 Lovelock, J. E.: Methyl chloroform in the troposphere as an indicator of OH radical abundance, *Nature*,
960 267, 32-32, 10.1038/267032a0, 1977.

961 Mao, J., Ren, X., Brune, W. H., Olson, J. R., Crawford, J. H., Fried, A., Huey, L. G., Cohen, R. C., Heikes, B.,
962 Singh, H. B., Blake, D. R., Sachse, G. W., Diskin, G. S., Hall, S. R., and Shetter, R. E.: Airborne measurement
963 of OH reactivity during INTEX-B, *Atmos. Chem. Phys.*, 9, 163-173, 10.5194/acp-9-163-2009, 2009.

964 Martínez-Alonso, S., Deeter, M., Worden, H., Borsdorff, T., Aben, I., Commane, R., Daube, B., Francis, G.,
965 George, M., Landgraf, J., Mao, D., McKain, K., and Wofsy, S.: 1.5 years of TROPOMI CO measurements:
966 comparisons to MOPITT and ATom, *Atmos. Meas. Tech.*, 13, 4841-4864, 10.5194/amt-13-4841-2020,
967 2020.

968 McPeters, R. D., Frith, S., and Labow, G. J.: OMI total column ozone: extending the long-term data
969 record, *Atmos. Meas. Tech.*, 8, 4845-4850, 10.5194/amt-8-4845-2015, 2015.

970 Miller, D. O., and Brune, W. H.: Investigating the Understanding of Oxidation Chemistry Using 20 Years
971 of Airborne OH and HO₂ Observations, *Journal of Geophysical Research: Atmospheres*, 127,
972 e2021JD035368, <https://doi.org/10.1029/2021JD035368>, 2022.

973 Miyazaki, K., Bowman, K. W., Yumimoto, K., Walker, T., and Sudo, K.: Evaluation of a multi-model, multi-
974 constituent assimilation framework for tropospheric chemical reanalysis, *Atmos. Chem. Phys.*, 20, 931-
975 967, 10.5194/acp-20-931-2020, 2020.

976 Miyazaki, K., Bowman, K., Sekiya, T., Takigawa, M., Neu, J. L., Sudo, K., Osterman, G., and Eskes, H.:
977 Global tropospheric ozone responses to reduced NO_x emissions linked to the COVID-19 worldwide
978 lockdowns, *Science Advances*, 7, eabf7460, 10.1126/sciadv.abf7460, 2021.

979 Montzka, S. A., Krol, M., Dlugokencky, E., Hall, B., Jockel, P., and Lelieveld, J.: Small Interannual
980 Variability of Global Atmospheric Hydroxyl, *Science*, 331, 67-69, 10.1126/science.1197640, 2011.

981 Murray, L. T., Mickley, L. J., Kaplan, J. O., Sofen, E. D., Pfeiffer, M., and Alexander, B.: Factors controlling
982 variability in the oxidative capacity of the troposphere since the Last Glacial Maximum, *Atmospheric*
983 *Chemistry and Physics*, 14, 3589-3622, 10.5194/acp-14-3589-2014, 2014.

984 Murray, L. T., Fiore, A. M., Shindell, D. T., Naik, V., and Horowitz, L. W.: Large uncertainties in global
985 hydroxyl projections tied to fate of reactive nitrogen and carbon, *Proceedings of the National Academy*
986 *of Sciences*, 118, e2115204118, 10.1073/pnas.2115204118, 2021.

987 NASA Goddard Space Flight Center. MERRA2 GMI, NASA [data set], [https://acd-](https://acd-ext.gsfc.nasa.gov/Projects/GEOSCCM/MERRA2GMI/)
988 [ext.gsfc.nasa.gov/Projects/GEOSCCM/MERRA2GMI/](https://acd-ext.gsfc.nasa.gov/Projects/GEOSCCM/MERRA2GMI/), last access: 6 March 2023.

989 Nault, B. A., Garland, C., Pusede, S. E., Wooldridge, P. J., Ullmann, K., Hall, S. R., and Cohen, R. C.:
990 Measurements of CH₃O₂NO₂ in the upper troposphere, *Atmospheric Measurement Techniques*, 8, 987-
991 997, 10.5194/amt-8-987-2015, 2015.

992 Naus, S., Montzka, S. A., Pandey, S., Basu, S., Dlugokencky, E. J., and Krol, M.: Constraints and biases in a
993 tropospheric two-box model of OH, *Atmos. Chem. Phys.*, 19, 407-424, 10.5194/acp-19-407-2019, 2019.

994 Naus, S., Montzka, S. A., Patra, P. K., and Krol, M. C.: A three-dimensional-model inversion of methyl
995 chloroform to constrain the atmospheric oxidative capacity, *Atmospheric Chemistry and Physics*, 21,
996 4809-4824, 10.5194/acp-21-4809-2021, 2021.

997 Nicely, J. M., Salawitch, R. J., Canty, T., Anderson, D. C., Arnold, S. R., Chipperfield, M. P., Emmons, L. K.,
998 Flemming, J., Huijnen, V., Kinnison, D. E., Lamarque, J.-F., Mao, J., Monks, S. A., Steenrod, S. D., Tilmes,
999 S., and Turquety, S.: Quantifying the causes of differences in tropospheric OH within global models,
1000 *Journal of Geophysical Research: Atmospheres*, JD026239, 10.1002/2016JD026239, 2017.

1001 Nicely, J. M., Duncan, B. N., Hanisco, T. F., Wolfe, G. M., Salawitch, R. J., Deushi, M., Haslerud, A. S.,
1002 Jöckel, P., Josse, B., Kinnison, D. E., Klekociuk, A., Manyin, M. E., Marécal, V., Morgenstern, O., Murray, L.
1003 T., Myhre, G., Oman, L. D., Pitari, G., Pozzer, A., Quaglia, I., Revell, L. E., Rozanov, E., Stenke, A., Stone, K.,
1004 Strahan, S., Tilmes, S., Tost, H., Westervelt, D. M., and Zeng, G.: A machine learning examination of
1005 hydroxyl radical differences among model simulations for CCMI-1, *Atmospheric Chemistry and Physics*,
1006 20, 1341-1361, 10.5194/acp-20-1341-2020, 2020.

1007 Oman, L. D., Douglass, A. R., Ziemke, J. R., Rodriguez, J. M., Waugh, D. W., and Nielsen, J. E.: The ozone
1008 response to ENSO in Aura satellite measurements and a chemistry-climate simulation, *Journal of*
1009 *Geophysical Research-Atmospheres*, 118, 965-976, 10.1029/2012jd018546, 2013.

1010 Orbe, C., Oman, L. D., Strahan, S. E., Waugh, D. W., Pawson, S., Takacs, L. L., and Molod, A. M.: Large-
1011 Scale Atmospheric Transport in GEOS Replay Simulations, *Journal of Advances in Modeling Earth*
1012 *Systems*, 9, 2545-2560, 10.1002/2017ms001053, 2017.

1013 Patra, P. K., Krol, M. C., Montzka, S. A., Arnold, T., Atlas, E. L., Lintner, B. R., Stephens, B. B., Xiang, B.,
1014 Elkins, J. W., Fraser, P. J., Ghosh, A., Hints, E. J., Hurst, D. F., Ishijima, K., Krummel, P. B., Miller, B. R.,
1015 Miyazaki, K., Moore, F. L., Muhle, J., O'Doherty, S., Prinn, R. G., Steele, L. P., Takigawa, M., Wang, H. J.,
1016 Weiss, R. F., Wofsy, S. C., and Young, D.: Observational evidence for interhemispheric hydroxyl-radical
1017 parity, *Nature*, 513, 219-223, 10.1038/nature13721, 2014.

1018 Pérez-Ramírez, D., Smirnov, A., Pinker, R. T., Petrenko, M., Román, R., Chen, W., Ichoku, C., Noël, S.,
1019 Abad, G. G., Lyamani, H., and Holben, B. N.: Precipitable water vapor over oceans from the Maritim
1020 Aerosol Network: Evaluation of global models and satellite products under clear sky conditions,
1021 *Atmospheric Research*, 215, 294-304, <https://doi.org/10.1016/j.atmosres.2018.09.007>, 2019.

1022 Pickett, H. M., Drouin, B. J., Canty, T., Salawitch, R. J., Fuller, R. A., Perun, V. S., Livesey, N. J., Waters, J.
1023 W., Stachnik, R. A., Sander, S. P., Traub, W. A., Jucks, K. W., and Minschwaner, K.: Validation of Aura
1024 Microwave Limb Sounder OH and HO₂ measurements, *Journal of Geophysical Research: Atmospheres*,
1025 113, D16S30, <https://doi.org/10.1029/2007JD008775>, 2008.

1026 Pimlott, M. A., Pope, R. J., Kerridge, B. J., Latter, B. G., Knappett, D. S., Heard, D. E., Ventress, L. J.,
1027 Siddans, R., Feng, W., and Chipperfield, M. P.: Investigating the global OH radical distribution using
1028 steady-state approximations and satellite data, *Atmos. Chem. Phys.*, 22, 10467-10488, 10.5194/acp-22-
1029 10467-2022, 2022.

1030 Rigby, M., Montzka, S. A., Prinn, R. G., White, J. W. C., Young, D., O'Doherty, S., Lunt, M. F., Ganesan, A.
1031 L., Manning, A. J., Simmonds, P. G., Salameh, P. K., Harth, C. M., Muhle, J., Weiss, R. F., Fraser, P. J.,
1032 Steele, L. P., Krummel, P. B., McCulloch, A., and Park, S.: Role of atmospheric oxidation in recent
1033 methane growth, *Proc Natl Acad Sci U S A*, 114, 5373-5377, [10.1073/pnas.1616426114](https://doi.org/10.1073/pnas.1616426114), 2017.

1034 Shah, V., Jacob, D. J., Dang, R., Lamsal, L. N., Strode, S. A., Steenrod, S. D., Boersma, K. F., Eastham, S. D.,
1035 Fritz, T. M., Thompson, C., Peischl, J., Bourgeois, I., Pollack, I. B., Nault, B. A., Cohen, R. C., Campuzano-
1036 Jost, P., Jimenez, J. L., Andersen, S. T., Carpenter, L. J., Sherwen, T., and Evans, M. J.: Nitrogen oxides in
1037 the free troposphere: implications for tropospheric oxidants and the interpretation of satellite NO₂
1038 measurements, *Atmos. Chem. Phys.*, 23, 1227-1257, [10.5194/acp-23-1227-2023](https://doi.org/10.5194/acp-23-1227-2023), 2023.

1039 Silvern, R. F., Jacob, D. J., Travis, K. R., Sherwen, T., Evans, M. J., Cohen, R. C., Laughner, J. L., Hall, S. R.,
1040 Ullmann, K., Crouse, J. D., Wennberg, P. O., Peischl, J., and Pollack, I. B.: Observed NO/NO₂ Ratios in
1041 the Upper Troposphere Imply Errors in NO-NO₂-O₃ Cycling Kinetics or an Unaccounted NO_x Reservoir,
1042 *Geophysical Research Letters*, 45, 4466-4474, <https://doi.org/10.1029/2018GL077728>, 2018.

1043 Spivakovsky, C. M., Yevich, R., Logan, J. A., Wofsy, S. C., McElroy, M. B., and Prather, M. J.: Tropospheric
1044 OH in a three-dimensional chemical tracer model: An assessment based on observations of CH₃CCl₃,
1045 *Journal of Geophysical Research: Atmospheres*, 95, 18441-18471, [10.1029/JD095iD11p18441](https://doi.org/10.1029/JD095iD11p18441), 1990.

1046 Stauffer, R. M., Thompson, A. M., and Young, G. S.: Tropospheric ozonesonde profiles at long-term U.S.
1047 monitoring sites: 1. A climatology based on self-organizing maps, *Journal of Geophysical Research:*
1048 *Atmospheres*, 121, 1320-1339, <https://doi.org/10.1002/2015JD023641>, 2016.

1049 Stevenson, D. S., Zhao, A., Naik, V., and Connor, F. M., Tilmes, S., Zeng, G., Murray, L. T., Collins,
1050 W. J., Griffiths, P., Shim, S., Horowitz, L. W., Sentman, L., and Emmons, L.: Trends in global tropospheric
1051 hydroxyl radical and methane lifetime since 1850 from AerChemMIP, *Atmos. Chem. Phys.*, 20, 12905-
1052 12920, <https://doi.org/10.5194/acp-20-12905-2020>, 2020.

1053
1054 Strahan, S. E., Duncan, B. N., and Hoor, P.: Observationally derived transport diagnostics for the
1055 lowermost stratosphere and their application to the GMI chemistry and transport model, *Atmos. Chem.*
1056 *Phys.*, 7, 2435-2445, [10.5194/acp-7-2435-2007](https://doi.org/10.5194/acp-7-2435-2007), 2007.

1057 Strode, S. A., Ziemke, J. R., Oman, L. D., Lamsal, L. N., Olsen, M. A., and Liu, J.: Global changes in the
1058 diurnal cycle of surface ozone, *Atmospheric Environment*, 199, 323-333,
1059 [10.1016/j.atmosenv.2018.11.028](https://doi.org/10.1016/j.atmosenv.2018.11.028), 2019.

1060 Susskind, J., Blaisdell, J. M., and Iredell, L.: Improved methodology for surface and atmospheric
1061 soundings, error estimates, and quality control procedures: the atmospheric infrared sounder science
1062 team version-6 retrieval algorithm, *Journal of Applied Remote Sensing*, 8, 084994,
1063 [10.1117/1.Jrs.8.084994](https://doi.org/10.1117/1.Jrs.8.084994), 2014.

1064 Thompson, C. R., Wofsy, S. C., Prather, M. J., Newman, P. A., Hanisco, T. F., Ryerson, T. B., Fahey, D. W.,
1065 Apel, E. C., Brock, C. A., Brune, W. H., Froyd, K., Katich, J. M., Nicely, J. M., Peischl, J., Ray, E., Veres, P. R.,
1066 Wang, S., Allen, H. M., Asher, E., Bian, H., Blake, D., Bourgeois, I., Budney, J., Bui, T. P., Butler, A.,
1067 Campuzano-Jost, P., Chang, C., Chin, M., Commane, R., Correa, G., Crouse, J. D., Daube, B., Dibb, J. E.,
1068 DiGangi, J. P., Diskin, G. S., Dollner, M., Elkins, J. W., Fiore, A. M., Flynn, C. M., Guo, H., Hall, S. R.,
1069 Hannun, R. A., Hills, A., Hints, E. J., Hodzic, A., Hornbrook, R. S., Huey, L. G., Jimenez, J. L., Keeling, R. F.,
1070 Kim, M. J., Kupc, A., Lacey, F., Lait, L. R., Lamarque, J.-F., Liu, J., McKain, K., Meinardi, S., Miller, D. O.,

1071 Montzka, S. A., Moore, F. L., Morgan, E. J., Murphy, D. M., Murray, L. T., Nault, B. A., Neuman, J. A.,
1072 Nguyen, L., Gonzalez, Y., Rollins, A., Rosenlof, K., Sargent, M., Schill, G., Schwarz, J. P., Clair, J. M. S.,
1073 Steenrod, S. D., Stephens, B. B., Strahan, S. E., Strode, S. A., Sweeney, C., Thames, A. B., Ullmann, K.,
1074 Wagner, N., Weber, R., Weinzierl, B., Wennberg, P. O., Williamson, C. J., Wolfe, G. M., and Zeng, L.: The
1075 NASA Atmospheric Tomography (ATom) Mission: Imaging the Chemistry of the Global Atmosphere,
1076 *Bulletin of the American Meteorological Society*, 103, E761-E790, 10.1175/BAMS-D-20-0315.1, 2022.

1077 Turner, A. J., Frankenberg, C., Wennberg, P. O., and Jacob, D. J.: Ambiguity in the causes for decadal
1078 trends in atmospheric methane and hydroxyl, *Proceedings of the National Academy of Sciences*, 114,
1079 5367, 10.1073/pnas.1616020114, 2017.

1080 Turner, A. J., Fung, I., Naik, V., Horowitz, L. W., and Cohen, R. C.: Modulation of hydroxyl variability by
1081 ENSO in the absence of external forcing, *Proc Natl Acad Sci U S A*, 115, 8931-8936,
1082 10.1073/pnas.1807532115, 2018.

1083 van Geffen, J., Boersma, K. F., Eskes, H., Sneep, M., ter Linden, M., Zara, M., and Veefkind, J. P.: S5P
1084 TROPOMI NO₂ slant column retrieval: method, stability, uncertainties and comparisons with OMI,
1085 *Atmos. Meas. Tech.*, 13, 1315-1335, 10.5194/amt-13-1315-2020, 2020.

1086 Veefkind, J. P., Aben, I., McMullan, K., Förster, H., de Vries, J., Otter, G., Claas, J., Eskes, H. J., de Haan, J.
1087 F., Kleipool, Q., van Weele, M., Hasekamp, O., Hoogeveen, R., Landgraf, J., Snel, R., Tol, P., Ingmann, P.,
1088 Voors, R., Kruizinga, B., Vink, R., Visser, H., and Levelt, P. F.: TROPOMI on the ESA Sentinel-5 Precursor: A
1089 GMES mission for global observations of the atmospheric composition for climate, air quality and ozone
1090 layer applications, *Remote Sensing of Environment*, 120, 70-83,
1091 <https://doi.org/10.1016/j.rse.2011.09.027>, 2012.

1092 Verhoelst, T., Compernelle, S., Pinardi, G., Lambert, J. C., Eskes, H. J., Eichmann, K. U., Fjæraa, A. M.,
1093 Granville, J., Niemeijer, S., Cede, A., Tiefengraber, M., Hendrick, F., Pazmiño, A., Bais, A., Bazureau, A.,
1094 Boersma, K. F., Bogner, K., Dehn, A., Donner, S., Elokhov, A., Gebetsberger, M., Goutail, F., Grutter de la
1095 Mora, M., Gruzdev, A., Gratsea, M., Hansen, G. H., Irie, H., Jepsen, N., Kanaya, Y., Karagkiozidis, D., Kivi,
1096 R., Kreher, K., Levelt, P. F., Liu, C., Müller, M., Navarro Comas, M., Piters, A. J. M., Pommereau, J. P.,
1097 Portafaix, T., Prados-Roman, C., Puentedura, O., Querel, R., Remmers, J., Richter, A., Rimmer, J., Rivera
1098 Cárdenas, C., Saavedra de Miguel, L., Sinyakov, V. P., Stremme, W., Strong, K., Van Roozendaal, M.,
1099 Veefkind, J. P., Wagner, T., Wittrock, F., Yela González, M., and Zehner, C.: Ground-based validation of
1100 the Copernicus Sentinel-5P TROPOMI NO₂ measurements with the NDACC ZSL-DOAS, MAX-DOAS and
1101 Pandonia global networks, *Atmos. Meas. Tech.*, 14, 481-510, 10.5194/amt-14-481-2021, 2021.

1102 Voulgarakis, A., Naik, V., Lamarque, J. F., Shindell, D. T., Young, P. J., Prather, M. J., Wild, O., Field, R. D.,
1103 Bergmann, D., Cameron-Smith, P., Cionni, I., Collins, W. J., Dalsøren, S. B., Doherty, R. M., Eyring, V.,
1104 Faluvegi, G., Folberth, G. A., Horowitz, L. W., Josse, B., MacKenzie, I. A., Nagashima, T., Plummer, D. A.,
1105 Righi, M., Rumbold, S. T., Stevenson, D. S., Strode, S. A., Sudo, K., Szopa, S., and Zeng, G.: Analysis of
1106 present day and future OH and methane lifetime in the ACCMIP simulations, *Atmospheric Chemistry and
1107 Physics*, 13, 2563-2587, 10.5194/acp-13-2563-2013, 2013.

1108 Wang, P., Piters, A., van Geffen, J., Tuinder, O., Stammes, P., and Kinne, S.: Shipborne MAX-DOAS
1109 measurements for validation of TROPOMI NO₂ products, *Atmos. Meas. Tech.*, 13, 1413-1426,
1110 10.5194/amt-13-1413-2020, 2020.

1111 Wells, K. C., Millet, D. B., Payne, V. H., Deventer, M. J., Bates, K. H., de Gouw, J. A., Graus, M., Warneke,
1112 C., Wisthaler, A., and Fuentes, J. D.: Satellite isoprene retrievals constrain emissions and atmospheric
1113 oxidation, *Nature*, 585, 225-233, 10.1038/s41586-020-2664-3, 2020.

1114 Wild, O., Voulgarakis, A., and Connor, F., Lamarque, J.-F., Ryan, E. M., and Lee, L.: Global
1115 sensitivity analysis of chemistry-climate model budgets of tropospheric ozone and OH: exploring model
1116 diversity, *Atmospheric Chemistry and Physics*, 20, 4047-4058, 10.5194/acp-20-4047-2020, 2020.

1117 Wolfe, G. M., Nicely, J. M., St Clair, J. M., Hanisco, T. F., Liao, J., Oman, L. D., Brune, W. B., Miller, D.,
1118 Thames, A., Gonzalez Abad, G., Ryerson, T. B., Thompson, C. R., Peischl, J., McCain, K., Sweeney, C.,
1119 Wennberg, P. O., Kim, M., Crouse, J. D., Hall, S. R., Ullmann, K., Diskin, G., Bui, P., Chang, C., and Dean-
1120 Day, J.: Mapping hydroxyl variability throughout the global remote troposphere via synthesis of airborne
1121 and satellite formaldehyde observations, *Proc Natl Acad Sci U S A*, 116, 11171-11180,
1122 10.1073/pnas.1821661116, 2019.

1123 Wolter, K., and Timlin, M. S.: El Niño/Southern Oscillation behaviour since 1871 as diagnosed in an
1124 extended multivariate ENSO index (MEI.ext), *International Journal of Climatology*, 31, 1074-1087,
1125 10.1002/joc.2336, 2011.

1126 Zhao, Y., Saunio, M., Bousquet, P., Lin, X., Berchet, A., Hegglin, M. I., Canadell, J. G., Jackson, R. B.,
1127 Hauglustaine, D. A., Szopa, S., Stavert, A. R., Abraham, N. L., Archibald, A. T., Bekki, S., Deushi, M., Jöckel,
1128 P., Josse, B., Kinnison, D., Kirner, O., Maréchal, V., Connor, F. M., Plummer, D. A., Revell, L. E., Rozanov, E.,
1129 Stenke, A., Strode, S., Tilmes, S., Dlugokencky, E. J., and Zheng, B.: Inter-model comparison of global
1130 hydroxyl radical (OH) distributions and their impact on atmospheric methane over the 2000-2016
1131 period, *Atmospheric Chemistry and Physics*, 19, 13701-13723, 10.5194/acp-19-13701-2019, 2019.

1132 Zhu, L., Jacob, D. J., Kim, P. S., Fisher, J. A., Yu, K., Travis, K. R., Mickley, L. J., Yantosca, R. M., Sulprizio, M.
1133 P., De Smedt, I., González Abad, G., Chance, K., Li, C., Ferrare, R., Fried, A., Hair, J. W., Hanisco, T. F.,
1134 Richter, D., Jo Scarino, A., Walega, J., Weibring, P., and Wolfe, G. M.: Observing atmospheric
1135 formaldehyde (HCHO) from space: validation and intercomparison of six retrievals from four satellites
1136 (OMI, GOME2A, GOME2B, OMPS) with SEAC⁴RS aircraft observations over the southeast US,
1137 *Atmospheric Chemistry and Physics*, 16, 13477-13490, 10.5194/acp-16-13477-2016, 2016.
1138

1139 Zhu, Q., Laughner, J. L., and Cohen, R. C.: Estimate of OH trends over one decade in North American
1140 cities, *Proc Natl Acad Sci U S A*, 119, e2117399119, <https://doi.org/10.1073/pnas.2117399119>, 2022a.

1141 Zhu, Q., Laughner, J. L., and Cohen, R. C.: Combining Machine Learning and Satellite Observations to
1142 Predict Spatial and Temporal Variation of near Surface OH in North American Cities, *Environmental*
1143 *Science & Technology*, 7362 - 7371, 10.1021/acs.est.1c05636, 2022b.
1144